Insight into contrasting patterns of sedimentation from shelf edge to base-of-slope on the Mozambique-Zambezi margin (17°30'S-20°S) during the last 40 ka

Bernard Dennielou, Inacio H. Guambe, Constantino P. Matsena, João A. Mugabe, Mussa Achimo, Gwenael Jouet

Marine Geology
September 2022, Volume 451, Pages 106886 (23p.)
https://doi.org/10.1016/j.margeo.2022.106886
https://archimer.ifremer.fr/doc/00789/90107/

Insight into contrasting patterns of sedimentation from shelf edge to base-of-slope on the Mozambique-Zambezi margin (17°30′S-20°S) during the last 40 ka

Dennielou Bernard [1, *], Guambe Inacio H. [1, 2], Matsena Constantino P. [1, 2], Mugabe João A. [2], Achimo Mussa [2], Jouet Gwenael [1]

[1] Univ Brest, CNRS, Ifremer, Geo-Ocean, F-29280 Plouzané, France
[2] Department of Geology, University of Eduardo Mondlane, Maputo, Mozambique

* Corresponding author : Bernard Dennielou, email address : bernard.dennielou@ifremer.fr

Abstract :

The pattern of sediment dispersal and the location of sediment depocentres on continental margins can be very complex in both space and time. We aim at investigating how significantly external and internal factors, such as river runoff, bottom current and sliding can deviate the sediment dispersal from a simplistic fully sea-level controlled spreading. In this study we examined the sedimentation at two transects across the Mozambique-Zambezi slope between 17°20S-20°S, where multibeam bathymetry, sub-bottom profiler data and sediment cores were acquired. The period investigated spans the last 40 cal ka BP with a focus on the contrast between the last glacial (lowstand) and the Holocene (highstand) periods. Results show contrasting patterns of sediment dispersal, deposition and preservation. Sea level fluctuation remains the main forcing and most of the sediment from the Zambezi River settled on the inner shelf since the last sea level rise. However, we found that two major depocentres have developed on the upper slope during the Holocene consequent to the interaction of bottom currents with seabed morphologies at the shelf edge and at the upper slope. Early Holocene sliding in the north-east and in the south-west upper slope is a secondary but yet major factor of sediment transfer to the deep domain. Identified preconditioning factors for sliding on the slope are related to lowstand sediment loading and fluid circulation on the upper slope, and erosion at the base of slope of a plastered drift. Triggering must be related to margin wide mechanisms such as changes in hydrostatic pressure and reorganisation of sediment dispersal, subsequent to the post-glacial sea level rise, or maybe a period of regional seismicity. Climatic conditions in the Zambezi River watershed during the Bolling-Allerod and Younger Dryas periods are recorded and imprinted on the upper slope in the form of a detrital rich layer and a prominent slope-wide high-amplitude reflector. All over the continental slope, plastering of sediment deposits by bottom currents is pervasive and shows a morphological continuum from erosional scours at the base of slope to sediment waves on the upper slope and a possible interaction between along and across slope transport processes. We conclude that, in addition to sea level, the interplay of external and internal factors such as oceanic circulation and sliding, together with margin morphology, lead to the development of unexpected depocentres on the continental slopes. Thus, the study of modern marine analogues is crucial to avoid misleading interpretation of fossil deposits in terms of paleo sea level and more generally of paleo-environmental conditions.

Highlights

► Early Holocene sliding occurred in contrasting morphological and sedimentary settings ► Expanded Holocene deposits on the upper slope related to interaction between bottom current and the morphology of the margin and of the seabed ► Continuum of sediment undulations ranging from scours to sediment waves from base of slope to upper slope ► Sedimentation contrast between Bolling-Allerod/Younger Dryas and Early Holocene periods visible as a high amplitude reflector

Keywords : Indian Ocean, Mozambique margin, Zambezi River, continental slope, contourite, turbidite, landslide, bottom current, sediment waves, scours, climate, sea level

1. Introduction

The sedimentary development of continental margins is roughly controlled by the interplay of accommodation and sediment supply (Payton, 1977; Van Wagoner et al., 1988). In this respect, sea level fluctuation has long been recognized as a major driver for the emplacement of sediment depocentres and as the pacemaker of the stratigraphic pattern and sediment composition of continental margins, especially during the late Pleistocene (Rabineau et al., 1998; Reeves et al., 2008; Simmons, 2012). However, the

thorough exploration of continental margins with increasingly resolving acoustic tools and efficient sampling devices (Curray, 2014) have unveiled that passive margins can be locally segmented into compartments with incredibly contrasted sedimentation patterns in space and time. Thus, there is growing evidence of a "non-straightforward" and non-unique role of sea level (Armitage and Covault, 2011), and that depocentres are, to a large extent, also controlled by (1) internal parameters such as the tectonic, morphological and sedimentological characteristics of margins impacting canyon emplacements, evolution and sliding; (2) external parameters such as along-shelf or slope transport of sediment by currents and their interaction with margin morphological features (Bernhardt et al., 2016; Boyd et al., 2008; Covault et al., 2007; Gaudin et al., 2006; Mazières et al., 2014; Normandeau et al., 2013; Rebesco et al., 2014). In this respect, the Mozambique margin (Fig. 1) is an interesting case study to investigate the patterns of sedimentation because it is fed by the Zambezi River, the major East-African river, and is characterised by an expanded shelf, narrowing to the south-west and to the north-east. Therefore, the emplacement and migration of depocentres is highly sensitive to sea-level fluctuations between glacial lowstands and interglacial highstands (Schulz et al., 2011; van der Lubbe et al., 2014). The margin is also exposed to vigorous surface to bottom oceanic circulation (de Ruijter et al., 2002; Penven et al., 2006; Ullgren et al., 2016, 2012) (Figs. 1 and 2) that drives slope sediment transport and plasters the seabed (Breitzke et al., 2017; Fierens et al., 2019; Flemming and Kudrass, 2018; Kolla et al., 1980; Miramontes et al., 2019b, 2021; Thiéblemont et al., 2019; Wiles et al., 2017). The margin is also affected by giant sliding (Deville et al., 2020). Surprisingly there is no evidence of a recent major canyon incision that would funnel sediment across the continental slope. These characteristics make the

Mozambique margin the ideal place to illustrate the interplay between these multiple factors of sediment dispersal on the development of a sedimentary margin.

This study focused on two transects, one to the north-east and one to the south-west, across the Mozambique margin from the outer shelf to the base of slope off the Zambezi River. Interpretation and integration of multibeam bathymetry, chirp sub-bottom profiler data and sediment cores provide a detailed view of the sediment deposition patterns and associated gravity and hydro-sedimentary processes over the past 40 ka. The aim is to characterise the pattern of sedimentation since the last glacial period with a focus on the expression of sliding and bottom-current deposits, and more generally, the interaction between seabed morphology disruptions with along and across slope sediment transport and deposit.

2. Study area: Geologic, sedimentary and oceanic settings and previous work

The Mozambican margin in the vicinity of the Zambezi river mouth, between 22°S and 15°30S, is a 900-km-long passive margin of classic morphology with a well-developed shelf reaching 135 km off Beira and 80 km off the Zambezi delta (Fig. 2). To the north, the shelf disappears by pinching out gradually to form, between 17°S and 15°30S, a 20-km-wide strip interrupted by the Primeiras and Segundas coral-reef pinnacles archipelago. To the south, the shelf narrows abruptly and disappears at the Bazaruto Archipelago.

Suspended sediment yields of south-eastern Africa rivers is currently rather low when compared to major world rivers (Walling, 1984). The Zambezi river sediment yield is in the order of 40 $t.km^{-2}.y^{-1}$, yielding a potential natural sediment load of 52 $Mt.y^{-1}$ from the ca. $1.3x10^6$ km^2 basin (Milliman and Meade, 1983; Walling, 1984), though most of it is currently trapped behind dams so the load exported to the ocean is

estimated at 20 $Mt.y^{-1}$ (Milliman and Meade, 1983). Other small river basins, from south to north, Save, Buzi, Pungwe, Licungo, and Ligonha rivers, represent only ca. 15% of the surface of the Zambezi basin.

A 2-km-thick, prograding deltaic system of the Zambezi River was established from the Oligocene to present (Ponte et al., 2019). Until the Middle Miocene, the sediment routing dominantly converged to the Zambezi valley and was then gradually also diverted into the Intermediate Basin (ponded) at the base of slope of the Zambezi margin (Fierens, 2019; Fierens et al., 2022). Detailed analysis of deposits shows scarce turbidites and reduced sedimentation along the Zambezi valley since Marine Isotopic Stage 10 (ca. 350 ka) consecutive to a shift of the depocentre onto the Zambezi margin and Intermediate basin (Fierens et al., 2020). During the Late Pleistocene, the dispersal of sediment onto the shelf and slope was controlled by sea-level fluctuations and consecutive seaward and landward migrations of depocentres. During the current highstand, sediments are dominantly deposited on the delta and prodelta and on the shelf (Schulz et al., 2011). During the last lowstand, ca. 20 cal ka ago, the Zambezi river mouth moved seaward to reach the shelf break that is currently at ca. 80-100 m water depth in the south. Sediments were funnelled into the shelf, incising the Chinde-Zambezi paleo-valley (Beiersdorf et al., 1980) and delivered onto the slope where glacial sedimentation rates were higher than during the Holocene (Schulz et al., 2011; van der Lubbe et al., 2014; Wiles et al., 2017). However, on the slope, there is no major canyon to funnel the Zambezi sediment towards the base of slope of the Zambezi valley. Only a few sharp and narrow incisions dissect the slope in front of the Zambezi delta. In the north, the slope is dissected by multiple gullies with the northernmost coalescing towards the Zambezi valley (Wiles et al., 2017). At the base of slope, between 20°-22°S and 16°-17°30S, deposits in the form of sedimentary lobes, in the continuity of canyon networks,

are attributed to gravity-driven processes such as turbidity currents (Thiéblemont et al., 2019).

Although increasing (Breitzke et al., 2017; Jouet and Deville, 2015; Miramontes et al., 2020; Wiles et al., 2017), multibeam bathymetry and sub-bottom profiler data remain scarce on the Mozambique margin, making identification of large-scale morphologic features challenging. In this respect, between 19°S-20°S, 10-km-wide and 200-m-deep, depressions on the upper slope were interpreted as canyons (Wiles et al., 2017). However, an extensive multibeam survey has clearly shown that depressions are actually related to a massive recent slope sliding with volumes up to 33 km^3 (Cattaneo et al., 2019; Deville et al., 2020), consistent with recurrent sliding during the Pleistocene (Ortiz et al., 2016; Thiéblemont et al., 2019). Abundant pockmarks, indicative of active circulation of fluids, characterise the slide scar area, and the adjacent stable slope (Deville et al., 2020). Several pockmarks, mostly on the upper slope, show active gas flares indicative of free gas and are interpreted as a preconditioning factor for sediment instability on the upper slope (Deville et al., 2020).

In the Mozambique Channel, oceanic circulation is strong enough to transport sediment and has been shaping the seabed since the Late Cretaceous (Castelino et al., 2015). An extensive panel of hydrodynamically controlled deposits and bedforms has been described with increasing detail since the 80s (Breitzke et al., 2017; Castelino et al., 2015; Droz and Mougenot, 1987; Fierens et al., 2019; Flemming and Kudrass, 2018; Kolla et al., 1980; Miramontes et al., 2020, 2019b, 2019a; Thiéblemont et al., 2019; Wiles et al., 2017). Surface and intermediate circulation consist of the southward flowing Mozambique Current (MC), which is the northern part of the Agulhas Current, the strongest Western Boundary current in the southern hemisphere (Figs. 1 and 2). The MC is rather discontinuous as it is characterised by trains of anticyclonic eddies that affect

the whole water column and can reach the seabed down to 3000 m deep (Breitzke et al., 2017; de Ruijter et al., 2002). Large eddies, up to 300 km in diameter, forming at a frequency of four per year (Schouten et al., 2003), are characterised by velocities up to 2 $m.s^{-1}$ on the surface and 0.50 $m.s^{-1}$ at 300 m deep (Ternon et al., 2014). The MC is evoked for the emplacement of a plastered drift along the Mozambique slope between 300 m and 700 m, characterised by a convex morphology, with a steep slope, up to 5°–6°, in its upper part at 300–400 m (Miramontes et al., 2020). It is also evoked for the emplacement of a contourite terrace, between 120 m and 300 m characterised by a gentle slope, below 2° and truncated reflections covered by sandy ripples (Miramontes et al., 2020). Coastward, the MC drives a counter-circulation loop on the shelf, leading to a coast-parallel flow that deflects the river plume (Siddorn et al., 2001) and transports sediment towards the northern shelf area (Fig. 2). At water depths less than 50 m it controls the emplacement of an inner shelf mud belt (Schulz et al., 2011) and (van der Lubbe et al., 2014), redrawn after Beiersdorf et al., 1980) (Fig. 2). This is as an extension of the subaqueous deltas as is the case of many other river deposits (Cattaneo et al., 2003; Hanebuth et al., 2015; Petruno et al., 2015). In the north-east, where the shelf is reduced, the mud is eventually exported onto the upper slope where Holocene sedimentation rates higher than during the late glacial are recorded (Schulz et al., 2011). It is argued that mud, rather sandy, also accumulates along the upper slope under the influence of the MC (Beiersdorf et al., 1980; Schulz et al., 2011; van der Lubbe et al., 2014). Deep circulation, ca. 1500-3500 m deep, is fed by Antarctic Intermediate Water (AAIW) and the North Atlantic Deep Water (NADW) masses entering from the south and flowing north to form the Mozambique Under Current (MUC) (Figs. 1 and 2). The MUC, with an average speed in the order of 5-10 cm s^{-1} and maximum speeds of 33–40 cm s^{-1} (Miramontes et al., 2019b; Ridderinkhof and de Ruijter, 2003), plasters the seabed, like

at the Beira structural high where a 10-km-wide moat and detached drift have developed (Wiles et al., 2017).

3. Methods and data

This study is based on multi-beam bathymetry, chirp sub-bottom profiler data (SBP) and sediment cores collected from two areas on the northern Mozambique margin during the PAMELA-MOZ4 cruise (Jouet and Deville, 2015). When the cruise was carried out, only scarce multi-beam bathymetry was available (Reichert and Aslanian, 2007) and data from other cruises external to the project were not yet published (Franke et al., 2014; Jokat, 2014). The strategy for data acquisition was thus basically driven by the will to explore the margin and tracklines are not ideally located or orientated with regard to the features and structures subsequently identified. Data were collected across the slope, in the north-east around 18°S-39°E at a water depth between 200 m and 2500 m, and along the upper slope at water depths between 100 m and 600 m in the south-west around 19°40S-36°40E (Figs. 2, 3 and 4).

Multibeam data was acquired with a Seabat 7150 echo sounder emitting at 24 kHz and 12 kHz frequencies; vertical sounding accuracy is undetermined but is commonly less than 0.2% of water depth for multibeam echosounders (Kongsberg Maritime AS, 2011). Bathymetry data were processed using Ifremer software CARAIBES and gridded at 50 m resolution. Reference sound velocity comes from measured temperature (Sippican) and estimated salinity (Levitus table), tide correction was applied from predicted tide. Acoustic backscatter data were processed using Ifremer software GLOBE™ (Poncelet et al., 2020) and gridded at 25 m resolution. SBP lines were acquired with an IXSEA ECHOES 3500 T7 SBP operating in chirp mode between 1.8–5.3 kHz ; vertical resolution is around 30-50 cm. Data were processed using Ifremer in-

house QC Subop software and exported to the IHS Kingdom Suite™ software for display and interpretation. In figures, the vertical scale was converted in depth using a sound velocity of 1500 $m.s^{-1}$.

Sediment cores were collected with a Calypso piston corer aboard R/V Pourquoi pas ?. Coring sites were targeted on stratigraphic and morphological features identified on acoustic data. Cores MOZ4-CSF13, MOZ4-CSF12 and MOZ4-CSF11 were collected along a NW-SE dip transect in the north-east Angoche area at 904 m, 1905 m and 2134 m depth, respectively. Cores MOZ4-CSF18 and MOZ4-CSF19 were collected in the Zambezi area at 410 m and 315 m depth respectively (Figs. 2, 3 and 4; Tab. 1). The piston corer was equipped with pressure and acceleration sensors on the trigger and on the weight that allowed measuring the relative movement of the core barrel and piston and to convert the depth-in-core in in-situ depth with the Cinema software (Bourillet et al., 2007) (cf. supplementary material). In this respect, we inferred that all cores were slighted under sampled and that penetration depth was 10 to 15% longer than the recovered length (Tab. 1). It was therefore possible to improve the correlation of lithofacies with SBP facies.

Lithofacies and sediment composition were determined after visual and haptic description, smear-slide observation, digital radiographs, grain-size analysis and continuous logging for physical properties, spectrophotometry and geochemistry. Radiographs were acquired with a Geotek-XCT providing a pixel size of 150 µm. Physical properties (gamma density, p-wave velocity, magnetic susceptibility) were acquired on both whole and split cores acquired with a Geotek-MSCL, magnetic susceptibility. Spectrophotometry was acquired with a Minolta CM 2600d with a measurement area of 8 mm and using a daylight illuminant (D65) and a 10° viewing angle (specular component excluded). XRF scanning was performed with an Avaatech XRF Scanner

using two voltages (10 kV and 30 kV). Elemental ratios are used to determine the relative abundance of biogenic carbonate and detrital sources (Ca/Fe) or relative grain-size fluctuations (Zr/Rb) (Constantinescu et al., 2015; Richter et al., 2006; Rothwell, 2006). Grain-size analysis was conducted every ca. 10 cm with a Malvern Mastersizer 3000 laser diffraction particle size analyser. Prior to analysis, samples were homogenised in a dynamic suspension for five minutes.

Chronostratigraphy is based on radiocarbon dating of foraminifera (Tab. 2). Calibration into calendar ages was made using Calib8.2 software (Stuiver et al., 2018) and the marine calibration curve Marine20 (Heaton et al., 2020) and a ΔR=45 SD=85 (Maboya et al., 2018; Southon et al., 2002) for reservoir age. Linear accumulation rates (LAR) were calculated by linear interpolation between dated depths.

This work was based on already published work sharing some of the data presented here. In the south-western area, Deville et al. (2020) present the characteristics of a giant slide and the expression and role of active fluid seepage in slope destabilization. Here, we focussed on the impact of the slide scar morphology on the sediment dispersion pattern. In the same area, Miramontes et al. (2020) highlight the role of geostrophic currents and internal waves in shaping the continental slope. Here, we discuss the marked contrast of sedimentation between this stable open slope area and the adjacent slide scar. In the same area, de Castro et al. (2021) provide a detailed analysis of a muddy hyperpycnite lithofacies in the upper slope sediment core MOZ4-CSF19 during the end of the Bølling-Allerød wet period. Here, we interpret and discuss the significance of these metric-thick deposits and their seismic expression on the upper slope. The data in the north-eastern area have never been published.

4. Results and interpretation

The 250-m-resolution grid of the south-west Indian Ocean Bathymetric Compilation (swIOBC) (Dorschel et al., 2018) shows an overall smooth morphology with the shelf break visible between 80-100 m. The new swath bathymetry data (20 to 40 m resolution grid) presented in this paper unveils complex morphologies. Because the two study areas are distant from each other and show radically different morphological and sedimentological characteristics, we have presented and interpreted the results from the two areas separately.

4.1 North-eastern slope area (38°10'E-39°10'E)

Canyons

Six canyons cut across the shelf break and slope (C1 to C7 in Fig. 3). The southwesternmost at 38°20'E consist of a cluster of five canyons among which three coalesce downstream (C1, C2, C3) and one shows a deeper intraslope head (C5). Faint or narrow elongated depressions, here called gullies, are visible (G1 to G4) but do not necessarily reach the slope break (G1 and G2). Gullies are fainter and more frequent to the north-east (Fig. 3). On the upper slope, canyons are in the order of 3 km wide, 300 m deep with an overall V-shape but show a several-hundred-metre-wide flat floor. Flanks are steep, commonly between 25-40°. Downslope, between 1500-2000 m water depth, canyons show fainter morphologies with a shallower depth in the order of 30 m, but are much wider, around 6-8 km. To the west, as only one canyon is visible in the mid-slope, we argue that the upslope canyon cluster has coalesced into a single conduit (C1-4, in Fig. 3). All over the slope, canyons left flank (east side), show thicker sediment accumulations than on the right flank (west side) (Figs 5 and 6B). Upslope, these

accumulations are pinching out to the east suggesting that the sediment source issued from the western canyons (Fig. 5B and C).

Erosional features

In addition to canyons, several kinds of erosional features are visible throughout the area. At the shelf break and upper slope, at around 38°42'E, the multibeam bathymetry unveiled a complex morphology characterised by multiple headscarps and incisions down to 1800 m water depth (Fig. 4 and 4A). These are indicative of sliding and show that upslope sediments have been evacuated (Figs 4, 7 and 8). Headscarps are several kilometres long with heights of 50 to 90 m and commonly show morphological steps characteristic of retrogressive sliding (Badhani et al., 2020; Baeten et al., 2014; Li et al., 2017). In the south-east (38°50'E), the open slope is not smooth and shows furrows or scours (ca. 5-10 m deep, 200-800 m wide) that overlap each over and virtually cover the whole open slope (Figs. 4 and 5A, 5C).

Transparent layers: Mass-transport deposits MTDs

Several areas along and across the slope show seismically transparent deposits. From upper (420 m) to mid-slope (1200 m), a transparent layer (TL1ne) starts at the base of a headwall and pinches out from ca. 10 m to ca. 2 m at 1200 m where its continuity is uncertain (Figs. 7A and 7B). On the upper slope, TL1ne extends at least 13 km to the north-east of the canyon/slide scar, (limit of dataset), where it is gradually unburied and reaches the surface (Cf. highlighted in yellow on Fig. 5A 5C). It may also extend at least 20 km to the south-west of the canyon/slide scar, on the upper slope (500-700 m, (Cf. highlighted in yellow on Fig. 5B) and mid-slope (2000 m, Figs. 6A and 6C) where a transparent layer up to 10 m thick is visible on the surface. However, the

genetic link is questionable because of a disruption by a canyon and slide scars (Figs 4, 5A and 5B).

Another transparent layer (TL2ne) starts against a headwall at 1800 m and extends down to 2100 m (Fig. 4). The layer is 20-30 m thick upslope and abruptly becomes thinner (5-15 m) between 1950 m and 2100 m (Fig. 8). Despite a gap in data, the headwall upslope of TL2ne seems to extend upslope at 1000 m. The rough morphology at the base of TL2ne suggests important erosion possibly related to the emplacement of the layer during sliding. The transparent deposits have filled the underlying depressions and the morphology at the top of the layer is smoother than at the base. However, swath bathymetry shows up to 5 m high and 250-m-large blocks on top of the layer (Fig. 8). In areas where the transparent layer sits, seabed morphology is smoother than on adjacent areas because the pre-slide seabed morphology characterised by undulations and scours have been obliterated by the emplacement of the transparent layer.

At the SBP, vertical resolution (~30-50 cm) core MOZ4-CSF13 (Fig. 9) has completely penetrated TL1ne (Fig. 7) and core MOZ4-CSF12 has penetrated TL2ne at the base of slope without reaching the underlying substratum (Fig. 8). In core MOZ4-CSF13, intervals with evidences of sediment deformation and reworking are found between 5.66 and 8.54 m. They show a) mottled greenish and brownish mud possibly corresponding to mudclasts in a muddy matrix (5.94-6.60 m), b) layered light greenish grey and dark brownish grey mud and with intercalations of very fine sand to silt layers with intervals where layers show a 30° inclination (6.60-8.54 m). These intervals have a higher gamma-density than the surrounding sediment, which is a common characteristic of reworked sediment in Mass-Transport Deposits (MTDs) (Dennielou et al., 2019; Dugan, 2012). In core MOZ4-CSF12 (Fig. 9), between 3.25 and 8.05 m, bioturbated grey

carbonated ooze (50 to 70% foraminifera and coccoliths) with faint inclined (30°) laminations are indicative of reworking or tilting. The straight and oblique contact with the overlaying sediment (foraminifera-rich mud) and the erosive contact with the underlying sediment (coarse foraminifera-rich mud) are further evidence of reworking. Mid-slope (core MOZ4-CSF13), dating in TL1ne gave ages of 35.9 cal ka BP and out of the radiocarbon range, and an age of 5.9 cal ka BP in the overlaying deposits. At the base of slope (core MOZ4-CSF12), dating in TL2ne gave ages of 33.5 cal ka BP at 0.10 m and 10.5 cal ka BP at 8.00 m. Age reversals are indicative of reworking and also show that both transparent layers are composed of glacial and post-glacial deposits.

The emplacement, seismic characteristics, lithofacies as well as dating of the transparent layers, and the conjunction with headwalls are evidence of sliding and downslope transport (Badhani et al., 2020; Haflidason et al., 2004). Therefore, we interpret TL1ne and TL2ne as mass-transport deposits (MTDs). TL1ne and TL2ne seem to correspond to two separate MTDs rooted on different headwalls (Figs. 3 and 4). They may however belong to a single retrogressive sliding because they both lie at the seafloor and both involved glacial and post-glacial deposits. Owing to the age determined at the base of stratified sediment overlying TL1ne (5.9 cal ka BP), sliding occurred between the early and mid-Holocene (between 10.5 and 5.9 cal ka BP).

Upslope to mid-slope sediment wedge

From the shelf break to mid-slope, a downslope pinching-out sediment wedge overlaps the transparent layer TL1ne. It has maximum thickness of ca. 20 m close to the shelf break to less than 5 m at 1100 m where it is interrupted by headwalls (Fig. 7). The SBP facies is stratified (SLxne) with thicker strata upslope. Two stacked units have been identified; SL1ne and SL2ne are separated by a sharp seismic unconformity evidenced

by erosional truncations (Figs. 7B and 7C). At the shelf break, it shows an overall wavy to sigmoid shape that is rooted on the rough morphology on the underlying substratum characterised by glide planes and headwalls. Sliding has affected the upslope and thickest part of the wedge as evidenced by the occurrence of a headscarp and a transparent layer (Fig. 7C). After sliding, sedimentation resumed with the same wedge pattern (Fig. 7C). Core MOZ4-CSF13 (Fig. 9) crossed this deposit that consists of homogeneous bioturbated brownish grey mud with 30-40% of foraminifera and coccolith (Ca/Fe = 0.15-0.25), less carbonated than downslope pelagic deposits (Ca/Fe = 1.0-20). Radiocarbon dating at the base of the lithofacies gave an age of 5.9 cal ka BP (Tab. 2) showing that the wedge was emplaced during the Late Holocene with LAR of 80 $cm.ka^{-1}$ between 5.9-0.9 cal ka BP and a maximum of 226 $cm.ka^{-1}$ between 0.9 cal ka BP and Present.

Undulation pattern in stratified deposits

Several types of undulation are visible both on the seabed morphology and in the stratified sediment between 1900 m and 2300 m (Figs. 5, 6, 7, 8 and 10). Their expression on the seabed appears discontinuous because the morphology is also cut across by channels and is partly obliterated by transparent deposits (Fig. 6). Although the SBP line is oblique to the slope, the bathymetry shows that from mid-slope to the base of slope, undulation crests seem parallel to the slope (Figs. 6 and 10). Between 1600 m and 1900 m water depth, undulation wavelength from bathymetric data range between of 2.7-1.1 km with wavelength decreasing downslope and height is less than 5 m (Fig. 6C). Undulations are dominantly asymmetrical. The gentle side faces upslope and is characterized by a bigger accumulation than on the steep slope, as suggested by strata thickness, leading to an overall upslope migration of the wave crests (Figs 6A and 6C).

Gentle (stoss) sides are between 0.5-1.0 km long and have a dip around 0.15°, steep (lee) sides are between 1.0-1.5 km long and have a dip around 0.44°. Between 1900 and 2000 m, seabed morphology is dominated by across-slope channels and ridges with undulations on the ridges and along-channel flanks (Figs 6A and 6B). Sediment accumulation, together with undulations, occurs preferentially on the eastern flank of channels while the western flank is erosional. Between 2000 m and 2100 m, undulations are slightly asymmetrical and also show an upslope migrating pattern with a wavelength between 0.5 km and 1 km and height up to 10 m (Fig. 10A and 10C). Gentle (stoss) sides are between 0.2-0.4 km long and have a dip between 0.91-1.68°, steep (lee) sides are between 0.3-0.6 km long and have a dip between 1.42-1.96°.

At the deepest part, to the east, between 2100 m and 2200 m, undulations form spoon-shaped or elongated amalgamated giant scours parallel to the slope with dimensions in the order of 2-5 km long, 1-2 km large and 20-40 m deep (Fig. 10A and 10B). In contrast to the other undulations, the morphology of the scours is dominated by an erosional pattern with a steep erosive downslope facing flank and a gentle upslope facing flank. On the SBP, the seabed high amplitude reflection in the scours is interpreted as hard ground or sandy deposits related to erosion or lag deposits (Dennielou et al., 2009) whilst the stratified facies between scours is interpreted as predominantly depositional processes (Fig. 10B). Deposits between the scours were sampled in core MOZ4-CSF11 (Fig. 9). Lithofacies consist dominantly of grey carbonate-rich ooze (60-80% foraminifera and coccolith). Radiocarbon dating gave late glacial ages (35.0 to 42.3 cal ka BP) with a LAR of 75 cm.ka^{-1}. Noteworthy is the age of 35.0 cal ka BP, found at the top of the core, suggesting that sediment by-pass or erosion has occurred between the scours since the last glacial period. Deposits are also characterised by eight coarse beds (silt to coarse sand) up to 5 cm thick (Fig. 9). The beds commonly show a

basal erosional contact and normal grading but are not overlapped by a muddy layer. Sand is dominantly composed of lithogenic material with a few shell fragments and vegetal debris. These intervals are interpreted as gravity deposits, possibly top cut-out fine-grained turbidites because muddy to clayey layers are absent (Stow and Piper, 1984).

4.2 South-western slope area (19°40S-36°40E)

Stable continental slope

Unlike in the north-east, this part of the margin does not display any canyons. Instead, it shows a margin-scale, smooth morphology on the upper slope with a deeper and abrupt shelf break around 105 m water depth (Fig. 11A). The seabed does not show evidence of sliding (Fig. 11A). However, two major morphological features are visible. A ca. 240-m-wide channel, up to 13 m deep and about 60 km long, runs along the upper slope at ca. 160 m water depth (Figs 11A and 11C). This erosional feature was interpreted as the result of interaction between the seabed and internal waves propagating in the pycnocline near the upper slope (Miramontes et al., 2020). At the shelf edge, between 100 m and 135 m water depth, the seabed shows a discontinuous rough morphology, up to 3 km wide, which runs more than 30 km along the slope (Fig. 11A and 11C). SPB data show a higher amplitude seabed reflector than in adjacent areas and an acoustic mask preventing sound penetration. This is indicative of high impedance and therefore of hard substratum. Detailed morphology shows that the structure is composed of multiple pinnacles about 150-350 m wide and 10-15 m high (Figs. 11C and 13C), which can be interpreted as a drowned coral reef plateau, possibly the last glacial analogue to those forming the Primeiras and Segundas Archipelago in the north-eastern

part of the margin. Between 135 m and 600 m water depth, across the slope, the SBP facies (SL1sw) is dominantly transparent with slight stratification, parallel to the seabed at mid-slope between 400 m and 600 m, pinching out between 400 and 135 m (Fig. 13C). It is overlapped by a thin, ca. 2 m thick high-amplitude interval (HL) that reaches the seabed. A prominent high amplitude reflector (R) with downslope increasing depth is traced throughout the Zambezi upper slope and lies at ca. 6 m depth at 315 m water depth (Figs. 13B and 13C). On the upper slope it is truncated by the incising channel and the erosive contourite terrace (Miramontes et al., 2020), while along slope it is interrupted at 19°35 S and 18°50 S by major slides rooted on the upper slope.

Core MOZ4-CSF19, 9.50 m long, 315 m water depth, has penetrated through the shallow stratified high amplitude interval (HL), crossed reflector R and penetrated the upper part of the SL1sw facies. Lithofacies varies accordingly to the SBP facies. At the top of the core, the shallow interval (HL) corresponds to 2-m-thick sequence of well-sorted coarsening sand (33 to 90%) characterised by a maximum median grain size of 153 µm. This interval of coarse sediment is dominantly composed of lithics (quartz, micas) with planktonic foraminifera and various shell fragments. Radiocarbon dating shows that it was deposited during the Holocene after 9.1 cal ka BP with a LAR of 33 $cm.ka^{-1}$. This lithofacies was interpreted as winnowed sediment reworked under enhanced bottom current and is a lithostratigraphic expression of a contouritic terrace described on the upper slope (100-300 m) (Miramontes et al., 2020; van der Lubbe et al., 2014).

The SL1sw facies corresponds to dominantly structureless muddy lithofacies characterised by a dominant proportion (80-90%) of fine lithics (clay, quartz, micas) and a low proportion of biogenic fraction (foraminifera, shell debris). Radiocarbon dating as well as correlation with magnetic susceptibility from core 64PE304-88 at a

similar location (van der Lubbe et al., 2014) and the deeper core MOZ4-CS17 (Zindorf et al., 2021) shows that the sequence was deposited during the Last Glacial Maximum, and during the last deglacial and sea-level rise period. Between 470 cm and 570 cm, the lithofacies is more lithogenic (low Ca/Fe ratio) and consists of nine silty-clay to silt layers (1-3 cm thick) sometimes showing reverse grading. This 1-m-thick interval is interpreted as muddy hyperpycnite (de Castro et al., 2021). Interpolation between bracketing radiocarbon dating and correlation with nearby dated sediment cores (van der Lubbe et al., 2014; Zindorf et al., 2021) allows to attribute the interval an age around the Bolling-Allerod, between ca. 14.8-12.8 cal ka BP (Fig. 13).

Slided continental slope

Further south-west, the overall smooth morphology is disrupted by slide scars and mass transport deposits rooted around 100-105 m water depth and extending along the margin over more than 30 km, beyond our dataset (Figs. 11A and 11B). The slide shows across-slope alternations of corridors and blocky ridges, several kilometres wide and up to 130 m deep (Fig. 13). Detailed presentation and analysis of this mass wasting morphology can be found in Cattaneo et al. (2019) and (Deville et al., 2020). Across-slide, SBP facies show marked contrasts between topographic highs and lows. On the highs, and on the adjacent stable slope, SBP facies SL1sw is stratified (Fig. 13A). It shows several high-amplitude reflectors and a gradual attenuation of sound penetration, in the order of 50 ms twtt. Outside the slide scar, facies, SL1sw is characterised by high-amplitude pinching-out reflections, as shown by truncated strata indicative of seabed erosion. In the slide scar, SL1sw facies is visible although less stratified than outside the scar. On the scar highs the SL1sw facies outcrops on the seabed, at least at the SBP resolution, suggesting that no sediment was deposited since the slide occurred. The slide

scar is filled by a layer (SL2sw) showing a draping pattern and characterised by a stratified to transparent facies with medium amplitude reflectors parallel to the morphology of the underlying substratum (Figs. 13A and 14). It fills the lows in the slide scar but is not observed close to the slide headwall at depths shallower than 240 m (Figs. 13). Its thickness ranges between 15 and 25 ms twtt (11-19 m) and becomes thinner to the east and downslope where the stratification vanishes and where the layer disappears around 700 m water depth. It is generally not observed along the highs (ridges) but can occur as thin deposits, in the order of a few milliseconds (less than 5 m), on some highs in the slide scar (Figs. 12A and 13).

Core MOZ4-CSF18, 9.41 m long, was collected in the slide scar at 410 m depth. It has penetrated throughout half of the SBP facies SL2sw (Fig. 13A). The lithofacies (Fig. 9) consists of homogeneous dark greenish-grey mud with dominant lithic fractions (quartz, micas) and a few shell fragments and foraminifera. Grain size distribution shows a low silty fraction and two modes at 4 µm and 69 µm. Both modes are very similar to grain-size lithics end members determined in the study area by (van der Lubbe et al., 2014) and confirm a dominantly lithogenic composition. The median grain size decreases gradually along the core from base to top and corresponds to a gradual increased abundance of the fine mode relatively to coarse mode. Radiocarbon dating (Tab. 2 and Fig. 9) gave a Holocene age of 6,8 cal. cal ka BP at the base of the core with sedimentation rates ranging between 116 $cm.ka^{-1}$ and 165 $cm.ka^{-1}$ (Tab. 2 and Fig. 9) which, if extrapolated to the base of facies SL2sw, suggests that draping in the slide scar started around 10.8 cal ka ago at the onset of Holocene. This age may therefore be the age of the slide. However, this is also the age attributed to the rapid flooding of the Mozambique shelf and retreat of the shoreline during the sea-level rise that followed the

Younger Dryas (YD) sea-level slowdown (Abdul et al., 2016; Bard et al., 2010) and lead to a major reorganisation in the sediment dispersal pattern (van der Lubbe et al., 2014).

5. Discussion

Considering the large extent of this Mozambique margin, our dataset is indeed too sparse to capture the full variability of along and across-slope morphologic and stratigraphic features, and sedimentary processes. This is particularly the case in the north-eastern area where the sediment wedge, slides and sediment waves are mostly imaged by only one or two track lines. This is insufficient to determine volumes or 2D lateral trends but suffices to adequately characterise sedimentary processes particularly with the support of ground-truthing by coring. These scattered evidences also allow to highlight the marked contrast in the sedimentation pattern between the north-eastern and south-western areas.

5.1 Imprint of climate-induced sedimentation changes in the sedimentary strata

Seismic is a powerful tool in visualizing sedimentary bodies and strata over hundreds of metres. On continental margins, the pattern and geometry of reflectors outline bounding surfaces and architectural elements that define sequences and provide information on the sedimentary dynamics forced by accommodation and the sedimentary flux (Vail et al., 1977). However, the significance of reflectors in stratified facies inside architectural elements, remains unknown because it relies on multiple factors, indeed related to sediment composition, but also post-depositional processes (Nittrouer and Kravitz, 1996; Weaver et al., 2006).

On the Zambezi slope, stratified layers (SL) as seen on SBP data, are frequent (Fig. 15). In the south-west area, our data show a prominent reflector (R) that lies at ca. 4-6 m

below the seafloor, and can be tracked between 150 and 900 m water depth along a distance of ca. 150 km to the north-east and up to 20 km across the Zambesi slope for a surface of around 2000 km^2 (Fig. 16). This suggests a major change in sedimentation that would have affected the whole margin. Several sediment cores (Schefuß et al., 2011; van der Lubbe et al., 2014; Zindorf et al., 2021), including our core MOZ4-CSF19 (Figs 9 and 15) have penetrated the reflector and show that it corresponds to 1-2-m-thick deposits characterised by high-magnetic susceptibility and a high Fe/Ca ratio interpreted as increased detrital input deposited at the end of the Bolling/Allerod and transition to the Younger Dryas.

To the south-west of the Zambesi mouth the detrital pulse occurred during the B/A (Fig. 15) (van der Lubbe et al., 2014), while to the north-east, it seems to have occurred later at the B/A-YD transition (Schefuß et al., 2011; van der Lubbe et al., 2016). It is attributed to wetter conditions in the Zambezi catchment (Schefuß et al., 2011) with a high Zambezi runoff (van der Lubbe et al., 2016). The occurrence of silt layers with reverse grading interpreted as muddy hyperpycnites in this interval in core MOZ4-CSF17 (de Castro et al., 2021), confirm the close relation with the Zambezi runoff and a direct export of river borne sediment onto the slope. Because seismic reflectors correspond to contrasts in the sediment impedance (i.e. in physical properties and composition), and owing to the SBP vertical resolution (ca. 30 cm), we argue that the high amplitude reflector marks the transition between the sediment deposited during the transition between the Bolling-Allerod and the Younger Dryas and the period of reduced sedimentation on the slope ensuing the flooding of the shelf during the meltwater pulse 1B sea-level rise (van der Lubbe et al., 2014). It is noteworthy that the reflector is less or not visible north of 18°50'S despite the occurrence of the detrital pulse in core GeoB9307 (Schefuß et al., 2011) (Fig. 16). This area is characterised by an

abrupt and shallow, shelf-slope transition and a steeper outer shelf that reduced the extension of the flooded shelf between the Bolling-Allerod (ca. 80 m water depth) and the beginning of the Holocene (ca. 40 m water depth) as shown in Fig. 16. As a result, the flooding of the shelf and sediment starvation of the upper slope occurred later in the north-west area and was delayed at ca. 10 cal ka BP (van der Lubbe et al., 2014), thus sustaining high sedimentation rates on the slope after the detrital pulse. We argue that in this area the sediment impedance contrast is too weak to generate the high amplitude reflector.

This outlines that climatic conditions in the Zambezi River watershed have significantly imprinted margin stratigraphy. The prominent reflector is therefore a remarkable slope-wide, 1-2-m-thick stratigraphic marker of the Bolling-Allerod and Younger Dryas climatic oscillation and ensuing sea-level rise. However, the reflector does not extend onto the outer shelf where it pinches out and is interrupted by an erosional channel, a dominantly erosional contourite terrace and outcropping carbonate reefs (Fig. 13) (Miramontes et al., 2020), suggesting that the energetic oceanic circulation may have hampered its preservation after the flooding of the shelf.

5.2 Thick Holocene muddy deposits on the upper slope, interaction between currents and seabed morphology

Further to the flooding of the Zambezi shelf after ca. 11 cal ka BP, the locus of sedimentation dominantly shifted from the slope onto the inner shelf with a deflection to the upper slope under cyclonic oceanic circulation (Schulz et al., 2011; van der Lubbe et al., 2014; Wiles et al., 2017). Our data confirm the development of important Holocene deposits on the upper slope in the north-east (Figs. 7 and 5C) and south-west areas (Fig. 13A). These match the location of the muddy deposits shown in Schulz et al. (2011) and

redrawn after (Beiersdorf et al., 1980). However, the two deposits show considerable differences in terms of shape, emplacement and composition.

In the north-east area, the dominantly detrital composition (Ca/Fe = 0,1) of the sediment wedge indicates a clear fluvial source. The sediment wedge pinches out downslope to the SE and to the NE (Figs. 5 and 7) showing that the sediment was advected from the south-west by the north-east clockwise flowing shelf circulation (Fig. 5) and that the wedge developed along the flow, along and across the slope as a consequence of the narrowing of the shelf (Schulz et al. 2011). Pinching-out deposits (Fig. 5C) mimic the underlying undulated pattern, further suggesting that bottom currents are the main forcing on these deposits, confirming therefore that the whole sedimentary body is a mud belt and more specifically a wedge mud belt *sensu* Hanebuth et al. (2015). Recent sliding at the thickest part of the mud wedge (Fig. 7) is interpreted as a consequence of the high accumulation rates that possibly occurred around 4-5 $m.ka^{-1}$ providing that sedimentation started after the flooding of the shelf at ca. 11 cal ka BP (van der Lubbe et al., 2014).

In the south-west, the muddy deposit (SL2sw) lies in the slide scar and is restricted to the lows in the scar showing that accumulation could not occur on the most elevated areas and was focussed in the scar depression. The morphology is that of a drape, but the deposit is thicker (20-25 m) around 400-600 m water depth to gradually become thinner (< 5m) around 700-800 m water depth. The high pelagic composition, calcareous nannoplankton ooze (Ca/Fe = 1), suggests that accumulation did not involve a dominantly detrital material, like in the north-east area, but mostly hemipelagic material from the adjacent slope. This muddy deposit contrasts remarkably with the high energy deposits of the adjacent slope characterised by an erosive channel and a low accumulation of coarse-grained contourite terrace indicative of high energy driven by

geostrophic currents (Miramontes et al., 2020). The slide scar therefore corresponds to a low energy area sheltered from the adjacent vigorous bottom current. The Holocene deposit in the scar may result from the focussing and accumulation of sediment winnowed from the adjacent slope. The deposit shows a slightly convex morphology with the thickest accumulation (20-25 m) at 400-600 m water depth which is also the depth where is located the maximum accumulation, on the plastered drift on the adjacent slope (Miramontes et al., 2020). Consequently, the deposit is not a mud belt because sediment deposition is not supplied by the advection of fluvial sediment. It belongs to the family of contourite drifts, similar to the adjacent plastered drift, but fed from winnowing of adjacent slope sediment to the north-east and whose morphology is controlled by the interaction of bottom currents, possibly low energy, with the slide scar rough morphology.

5.3 Post-glacial concomitant varied size slides at the Zambezi margin

Landsliding is a geological process widespread on continental margins and contributes to the dispersal of sediment (Masson et al., 2006). Landslides show a great variety of size and distribution in time. This is the consequence of the complex interaction between several preconditioning conditions and triggering mechanisms. On a global scale, their timing and emplacement shows random distribution with no robust statistical correlation with sea-level fluctuation or rapid slope sedimentation (Urlaub et al., 2013), therefore making it difficult to attribute straightforward causes. The Zambezi margin extends over 600 km and exhibits abundant slides or Mass Transport Deposits mostly during and after the Mid-Pleistocene Transition, possibly correlated to glacial marine regressions (Ortiz et al., 2016). In the two study areas, recent subsurface slides and slope sedimentation show striking differences, but also similarities, questioning the

interplay between preconditioning factors and triggering mechanisms leading to sliding on this margin.

Differences

- A difference lies in the volume of sediment involved in sliding. In the south-west area, the margin shows one well-developed scar, up to 100 to 150 m high and 50 km long (Cattaneo et al., 2019; Deville et al., 2020), and in the north-east area it shows several nested scars, 10 to 90 m high and up to 20 km long (this study). These characteristics suggest that the volume involved in the mass wasting was four times superior in the south-west area.
- A difference lies in the slope gradients of the upper slope with a lower average slope of 3° in the south-west area and a higher average slope of 5° in the north-east area between 200 m and 1000 m water depth.
- A difference lies in the sedimentation rates of the two areas. In the south-west area, sedimentation rates range between 1-2 $m.ka^{-1}$ at a water depth between 300-600 m during the last glacial and early deglacial periods before shelf flooding (Fig. 9) (van der Lubbe et al., 2014; Zindorf et al., 2021). The rates decrease gradually to the north-east to less than 0.5 $m.ka^{-1}$ at 18°15'S (van der Lubbe et al. (2014) and 0.1 $m.ka^{-1}$ around 17°45S (Schulz et al., 2011; Van Campo et al., 1990). This suggests even more reduced mid-slope sedimentation rates in our north-east study area, in relation to depleted detrital input as shown by the foraminifera ooze deposits at the base of slope (core MOZ4-CSF11, Fig. 9). This is consistent with the shift of the Zambezi river depocentres into the intermediate basin, to south-east of the Mozambique margin during the Late Pleistocene (Fierens et al., 2020) .

- A difference lies in the occurrence of pervasive fluid seepages and pockmarks along the south-western margin but not in the north-east area. They are interpreted as the expression of fluid overpressure related to the huge accumulation of sediments below the Zambezi platform (Deville et al., 2020). It was shown that the south-west sliding is a gradual, maybe ongoing, process as suggested by the gradual change in seabed morphology between the adjacent stable area and the slide (Deville et al., 2020).

Similarities

- The subsurface morphology of both slides shows that sliding is recent in both areas because scars are not buried. This is confirmed by the extrapolated early Holocene age (10.8 cal ka BP) of the drape sealing the slide in the south-west area and by the occurrence of early Holocene (10.5 cal ka BP) material involved in the TL2ne, and the mid-Holocene age (5.9 cal ka BP) at the base of sediment wedge overlapping TL1ne in the north-east area(Fig. 9).
- Regarding the age of destabilized material, in the north-east area the sediment involved in the TL1ne is older than 43.5 cal ka BP (Fig. 9), and of glacial (3.4 cal ka BP) to early Holocene (10.5 cal ka BP) ages in the TL2ne (Fig. 9). In the south-west area, the chronostratigraphy of adjacent stable material (Fig. 9 and van der Lubbe et al., 2014 and Zindorf et al., 2021) shows that a similar late glacial age to early Holocene (10.8 cal ka BP) ages can be expected for the destabilized material (Figs 13 and 14).

Despite drastic different preconditioning factors in terms of slope gradient, sedimentation rate and fluid circulation, the two areas experienced sliding at the same period of time and for the same stratigraphic interval. This raises the question of

common preconditioning or triggering mechanisms that can affect simultaneously the whole margin. Three mechanisms meet the criteria: (1) the last glacial sea-level rise, which drove changes in sediment hydrostatic pressure and (2) in the sediment dispersal pattern with the post-glacial onset of sediment starvation on the slope and erosion on the upper slope and possibly at the base of slope under vigourous bottom current movement; (3) earthquakes that can shake the whole of the margin and modify pore pressure and sediment strength. Our data do not permit to solve this issue but their pertinence could be discussed in the light of sedimentological and geological settings.

The fact that sliding occurred in both areas around the end of the last deglacial sea-level rise suggests that water loading has played a role. Water loading during sea-level rise can generate transient excess pore pressure, therefore reducing sediment strength and leading to failure (Smith et al., 2013). This process is invoked as triggering mechanisms, particularly on slopes where excess pore pressure related to high sedimentation rates (Sultan et al., 2004) is further increased by water loading (Smith et al., 2013; Trincardi et al., 2003). This triggering mechanism would perfectly apply to the south-western area slope slide where fluid migration and seepages are interpreted as a preconditioning or even a triggering mechanism of the megaslide slide (Deville et al., 2020). One can argue that the last sea level rise acted as the external triggering mechanism, providing the last "kick" to the sediment already close to failure. This mechanism does not apply to the north-eastern slides characterised by low glacial sedimentation rates (i.e. reduced sediment load) and no evidence of excess pore pressure and fluid migration.

The post-glacial change in sediment dispersal drastically increased sediment loading in the north-east area during the Holocene highstand. This is evidenced by the development of a wedge mud belt on the upper slope (Fig. 7). Thus, although sediment

loading was significantly lower than in the south-west area of the margin during the lowstand, the increase during highstand, together with the concomitant decrease in the south-west area, may have rebalanced preconditioning by sediment loading over the margin and thus the sensitivity to external trigger mechanisms. This may however have had a limited impact, because the development of the mud wedge occurred mostly after the sliding (Fig. 7).

Sliding is very common in contouritic deposits regardless of the latitude or sediment composition (Laberg and Camerlenghi, 2008; Miramontes et al., 2018). The convex shape of drifts develops areas of high slope gradient where sliding may initiate. This is particularly the case in plastered drifts where the deep water part of the drift commonly shows a moat characterised by a high slope gradient and reduced sedimentation rates or even erosion, making this area the most prone to fail (Miramontes et al., 2018). The plastered drift that develops along the Mozambique slope shows steep flanks and a moat around 2800 m water depth formed by the MUC (Wiles et al., 2017). Although this bottom current was probably perennial throughout glacial and interglacial periods, the water-mass interfaces have fluctuated. The NADW is an important component of the MUC (Miramontes et al., 2019b)(Fig. 1). It was reduced during the last glacial because of decreased deep water formation in the North Atlantic (Bergh et al., 2021), and was possibly replaced by the northward extension of a less vigorous Antarctic Bottom Water (AABW) (Breitzke et al., 2017) (Fig. 1). Thus, the post-glacial reactivation of vigorous bottom circulation at the base of the Mozambique slope may have enhanced erosion and developed favourable prerequisite conditions for sliding. It is however too bold to consider that an enhanced post-glacial erosion at the base of slope may be the margin scale triggering mechanism of the early Holocene slides in the north-east and south-west areas.

To the north of the study area, offshore Tanzania, tectonic movements and earthquake swarms related to the East African Rift System (EARS) played a major role in the routing of the deep-water drainage network during the Cenozoic (Dottore Stagna et al., 2022; Maselli et al., 2020b). Large-scale mass wasting during the early-mid Miocene is coeval with cratonic rifting in Tanzania and attributed seismicity and enhanced sediment supply (Maselli et al., 2020a). The Mozambique-Zambezi margin is surrounded by faulted and seismogenic areas that constitute the southern extension of the western branch (onshore) and eastern branch (offshore) of the EARS (Deville et al., 2018; Franke et al., 2015; Grimison and Chen, 1988) (Fig. 1). The offshore seismogenic areas extend from the Davie Ridge to the Eparse Islands and correspond to an active fault array that reaches the seabed (FIg. 1) (Deville et al., 2018). Western and Eastern EARS earthquakes, with magnitudes up to 7 may thus have exerted a control on the trigger of Holocene landslides on the Mozambique-Zambezi margin despite a distance exceeding several hundred kilometres. It has however been pointed out that the passage of seismic waves from remote earthquakes of magnitude 5.5 are able to trigger submarine landslides at a distance as far as 1600 km (e.g. Gulf of Mexico, Fan et al., 2020), suggesting therefore that EARS seismicity likely exerted a control on recent mass wasting on the Mozambique-Zambezi margin like offshore Tanzania. However, because shaking from distant earthquakes must be homogenous throughout the study area, it discards the likeliness of simultaneous failures of areas with drastically different sedimentary settings and preconditioning factors like the north-eastern and south-western areas. Because the two areas show very contrasted morphological and sedimentological settings, it is thus difficult to find a common triggering mechanism for the slides. However, it has been pointed out that large slides commonly occur in high sedimentation rate settings (Talling et al., 2014), and Stoecklin et al. (2017) show that

the occurrence and size of slides is actually controlled by the slope sedimentation rate. For a given sediment type on a given slope, in the case of thick accumulation, the gradual loss of permeability of the sediment will result in overpressure that increases more rapidly in high accumulation rate settings (Sultan et al., 2004). Thus, effective stress will increase at a slower rate with depth whereas shear stress will continue to increase proportionally to the deposited mass, leading to intervals weaker than those close to the surface (Stoecklin et al., 2017). In the case of shaking by an earthquake, failure will occur at the weakest layer that will be deep in the case of a high accumulation rate, like in the south-western area and shallow in the case of a low accumulation rate like in the north-western area. This process pleads therefore in favour of earthquake triggering in a context of favourable preconditioning factors.

5.4 Imprint of bottom current, from sediment waves to scours

Between 1500 m and 2200 m, undulations seem to form a continuum with scours and short wavelength sediment waves in the deeper area and long wavelength sediment waves in the shallow area. Both sediment waves and scours are parallel to the slope, raising the question of a common forcing, possibly related to bottom current running across the slope. Such seabed morphologies can be formed beneath geostrophic flows and turbidity currents (McCave, 2017) and show a wide range of size and characteristics (Symons et al., 2016). Sediment waves with 2 km wave length (1850 m) were sampled in the nearby 12.6 m long sediment core MD79-254 (Schulz et al., 2011; Van Campo et al., 1990). Because no lithologic description was provided, it was not possible to say if deposits related to turbidity currents exist. However, continuous chronostratigraphy based on oxygen isotopes of *globigerinoides rubber* (white) shows an average sedimentation rate of 4.8 $cm.ka^{-1}$ over the last 260 ka (Lemoine, 1998) and suggests a

dominantly hemipelagic sedimentation. Extrapolation of chronostratigraphy shows that sediment waves developed during the Pleistocene, at least during the last 1 Ma and are therefore related to a perennial hydrodynamic process. They could find their source in lee waves (Flood, 1988) related to the interaction between the northward flowing MUC formed by the AAIW and AABW and the seabed morphology . The wave crests are roughly parallel to the slope and the upslope migrating pattern suggests the contribution of downslope bottom current, not compatible with the expected overall along-slope bottom circulation. However, sediment wave formation by lee waves is a complex process that involves both across and along crest currents that can lead to sediment wave crests oblique to the bottom current (Blumsack, 1993; Blumsack and Weatherly, 1989). Furthermore, in the Mozambique channel, bottom circulation is an unsteady phenomenon with contribution from surface circulation in the form of eddies that can affect the whole water column, reach the seabed with high velocities and even revert the northward transport related to the MUC (de Ruijter et al., 2002; Miramontes et al., 2019b; Schouten et al., 2003, Ulgren et al., 2012). Sediment wave crests parallel to the slope may thus be compatible with the complex fluctuating bottom current pattern in the area. Downslope decreasing wavelength may correspond to a growing angle between the wave crest and the local mean flow orientation (Blumsack and Weatherly, 1989).

Giant scour fields as described here are common features at the base of slopes worldwide (Bonnel et al., 2005; Carvajal et al., 2017; Macdonald et al., 2011; Symons et al., 2016; Wynn et al., 2002) including the Mozambique margin (Breitzke et al., 2017). They are commonly associated with turbiditic channel terminations and interpreted as forming after a hydraulic jump or flow relaxation related to flow expansion or a break in slope (Pohl et al., 2019; Symons et al., 2016) and may form from flows that are only

weakly supercritical, cf. Symons et al. (2016). Indeed, the occurrence of turbidites in the sediment between the scours, thought infrequent, together with scour orientation suggests that across slope sediment-laden flows (turbidity currents) are involved in seabed scouring. The source of turbidity currents remains speculative but several small canyons and gullies on the upper slope (Fig. 3) suggest that sediment-laden flows have occurred across the slope. Furthermore, slides commonly evolve into turbidity currents at the base of slope (Clare et al., 2014; Piper et al., 1999), therefore recurrent slides and MTDs upslope the scour field (Figs 4, 5, 7 and 8) may have evolved into turbidity currents at the base of slope. The actual low number of turbidites found in the scour field (only eight during the last glacial period) is consistent with upslope recurrent sliding but also with the overall scarcity of terrigeneous sedimentation in the north-east area of the Mozambique margin during the Late Pleistocene (Fierens et al., 2020). There is an apparent continuity between the scours and the adjacent field of sediment waves to the west (Fig. 10). The evolution of turbidity current is driven by the slope gradient and particularly by abrupt changes in the slope gradient (Meiburg and Kneller, 2010; Pohl et al., 2020). As already evoked (Symons et al., 2016), we argue that a seabed with pre-existing short wavelength sediment wave morphology could drive local accelerations and decelerations of across slope turbidity currents. Flow characteristics, changing alternatively from critical to supercritical with sequences of deposition and erosion and hydraulic jumps would lead to the development of the field of scours rooted on a pre-existing field of sediment waves.

5.5. Atypical sediment depocenter on the Zambezi margin: Where and when?

Sediment is deposited nearly everywhere and at any time on continental margins. However, the locus and volume of deposition vary greatly with the distance to the

sediment source, accommodation, energy in the water column and seabed morphology. On the Mozambique margin, sea-level fluctuation is the major control on the location of main depocenters. Deposition occurs dominantly on the upper slope during sea-level lowstand, when the shelf is exposed and the Zambesi mouth is close to the outer shelf, and dominantly on the inner shelf during sea-level rise and highstand when the shelf is inundated (Schulz et al., 2011; van der Lubbe et al., 2014). Bottom current is a secondary but significant control on slope sediment dispersal as evidenced by the development during the highstand of an erosional terrace on the upper slope and of a plastered drift mid-slope (de Castro et al., 2021; Miramontes et al., 2020; Thiéblemont et al., 2019) and of a mud belt along the inner shelf (Beiersdorf et al., 1980; Schulz et al., 2011). In addition, though our data do not cover the whole Zambezi margin and are restricted to the sediment penetrated by short sediment cores and SBP seismic, we show that the morphology of the shelf and of the seabed also substantially control the pattern of sediment dispersal.

In the north-east, the narrowing of the margin to less than 30 km limits the lateral expansion of the mud belt so that sediment is diverted onto the upper slope (Beiersdorf et al., 1980; Schulz et al., 2011). This led to the emplacement of an, at least, 50-m-thick wedge mud belt that developed onto the upper slope during the Holocene (Fig. 7). Such developed deposit is commonly restricted to lowstand periods owing to the proximity of the upper slope and river mouth (Rabineau et al., 2005; Sierro et al., 2009). It is noteworthy that the sediment wedge exhibits slide scars, showing that mass wasting occurred during the early Holocene, concomitant to the development of the wedge and possibly sediment loading (Fig. 7), which is also a common characteristic of continental slopes during lowstand sediment loading (Badhani et al., 2020). This atypical emplacement on the north-east Mozambique upper slope is indeed a consequence of the

narrow shelf but, above all, it lies on the development of a north-east extension of the Zambezi subaqueous delta "mud belt" under vigorous coastal circulation. Thus, the mud belt acts as a river-borne sediment point source exported onto the upper slope, a similar configuration to that along most of the Zambezi upper slope during lowstands.

To the south-west, the origin of the thick Holocene deposit on the upper slope (Figs. 12, 13 and 14) lies in the focussing and trapping of sediment in the slide scar by bottom currents. The relative high biogenic and low lithogenic content pleads for a source from the winnowing of hemipelagic sediment from the adjacent northern slope by the MC to the north-west. This conjunction, already described on the Israeli margin (Ashkenazi, 2021), led to an atypical and significant locus of Holocene deposit on the upper slope. This kind of deposit, characterised by Holocene continuous high-rate sedimentation and high biogenic content is rather uncommon on upper slopes and holds therefore great potential for paleoenvironmental studies.

6. Conclusions

We examined the sedimentation pattern in the south-west and north-east of the Zambezi upper slope to base of slope during the last glacial, deglacial and Holocene periods. Although sea level is the dominant control on the deposits, we show contrasted patterns that are a direct consequence of bottom currents, climate and sliding (Fig. 17). We show that:

- The Zambezi margin exhibits Holocene expanded sedimentation loci on the upper slope that are atypical for a wide-shelf river-fed margin during highstands. On the north-east upper slope it shares features such as sediment loading and sliding that are common characteristics of lowstand river-fed slopes (Badhani et al., 2020), but here this happened during the Holocene and it is a direct

consequence of oceanic circulation along the inner shelf. The south-west hemipelagic deposit trapped in the slide scar is a real outsider with regard to sequence stratigraphy principles and is a consequence of the interaction between oceanic circulation and seabed morphology. These deposits outline the significant role played by bottom currents in dispersal on continental margins, in such a way, that it can mimic lowstand deposits on the upper slope or enhance accumulation when interacting with seabed morphological irregularities. Similar deposits on outcrops with scarce paleoenvironmental constraints may mislead the interpretation in terms of paleo sea level.

- Though the fluctuations of sea level controlled the emplacement of deposits on the slope, bottom current exerts a significant control on the pattern of deposition. These formed upslope migrating large sediment waves that developed over several climatic cycles, consequently displaying the perennial and steadiness of bottom current on the Zambezi margin during the Late Pleistocene. Bottom current may have also involved occasional sediment laden bottom current during the last glacial as evidenced by the occurrence of turbidites and scours at the base of slope.
- The contrast between deposits during the Bolling-Allerod to Young Dryas climatic instability (detrital rich interval, including silty to sandy layer with reverse grading), and deposits during the subsequent sediment starvation during the ensuing sea-level rise (hemipelagic) is imprinted in the upper slope sediment in the form of a prominent high amplitude slope-wide reflector. This outlines that this period of climatic oscillation in the Zambezi River watershed has significantly imprinted the margin stratigraphy, making this period of time a remarkable margin wide stratigraphic marker.

- Both the south-west and northeast areas recorded sliding during the early Holocene and both sliding events involved glacial sediment, despite contrasted morphological and sedimentological settings. The post-glacial sea-level rise could be the main actor in sliding through several preconditioning factors and may be the triggering mechanism related to the reorganisation of sediment dispersal. Though this remains speculative, triggering by a period of intense seismicity can be envisaged.

This study shows how complex sediment dispersal on continental margins can be when sea-level fluctuation, bottom current, sliding as well as contrasting margin morphologies are involved. It highlights that important volumes of sediment, expected to deposit on the shelf during highstands (Holocene), can be deflected onto the upper slope. We concur with the conclusion of Wiles et al. (2017) that such along-strike variations in margin sedimentation are not recognized in generalised sequence stratigraphic models. Thus, it shows that marine geology and the detailed study of modern analogues is crucial to avoid misleading interpretation of fossil deposits in terms of paleo-sea level and more generally of paleo-environmental conditions.

Acknowledgements

We carried out this study in the framework of the PAMELA project led by IFREMER and TotalEnergies in collaboration with IFP Energies nouvelles, Université de Bretagne Occidentale, Université de Rennes 1, Sorbonne Université and CNRS. We thank the captain and crew of the PAMELA-MOZ4 cruise aboard R/V Pourquoi pas ? and the technical staff of IFREMER for their help in data acquisition. Bathymetry data from cruise MD163-MOBAMASIS was provided courtesy of the Alfred Wegener Institut, Hemholtz Centre for Polar and Marine Research. This study was initiated during an

internship by IHG and CPM at IFREMER. They wish to thank Jeanne Vivet (French Ambassy in Mozambique) and Sylvia Barone (IFREMER) for support in organising their travel and stay at IFREMER. We thank Katherine L. Maier, an anonymous reviewer and Guest Editor Vittorio Maselli whose reviews significantly improved the manuscript. We thank Alison Chalm for the careful polishing of the English.

Data availability

The numerical dataset, processed multibeam bathymetry and SBP, (Jouet and Deville, 2015) collected during the oceanographic cruises of the PAMELA project (Bourillet, et al., 2013, https://doi.org/10.18142/236) are stored at SISMER data repository (http://en.data.ifremer.fr/SISMER or https://doi.org/10.17600/15000700). Sediment cores collected offshore Mozambique are curated at CREAM, the IFREMER core repository in Plouzané (France). Core data related to this article can be requested at: MOZ4-CSF11 http://igsn.org/BFBGX-85854; MOZ4-CSF12 http://igsn.org/BFBGX-85860; MOZ4-CSF13 http://igsn.org/BFBGX-85861; MOZ4-CSF18 http://igsn.org/BFBGX-128003; MOZ4-CSF19 http://igsn.org/BFBGX-128004. Access to these data is however restricted and has to be accepted by the partners of the PAMELA project. The industrial seismic data are licensed multiclient data. Access to this dataset has to be directly negotiated with the seismic contractors.

References

Abdul, N.A., Mortlock, R.A., Wright, J.D., Fairbanks, R.G., 2016. Younger Dryas sea level and meltwater pulse 1B recorded in Barbados reef crest coral Acropora palmata. Paleoceanography 31, 330–344. https://doi.org/10.1002/2015PA002847

Armitage, D.A., Covault, J.A., 2011. "Exceptional" Turbidite Systems in High-Latitude and Tectonically Active Settings and the Obsolescence of Ubiquitous Sequence Stratigraphic Models. Houston Geological Society Bulletin 53, 47–48. http://search.datapages.com/data/HGS/vol53/v53no7/images/vol53no7p47.pd

f ;
http://www.searchanddiscovery.com/pdfz/documents/2010/30122armitage/ndx_armitage.pdf.html

Ashkenazi, L., 2021. Foraminifera as indicators for recent sediments transport in the Eastern Mediterranean upper slope, offshore Israel (Master of Science). Ben-Gurion University of the Negev.

Badhani, S., Cattaneo, A., Dennielou, B., Leroux, E., Colin, F., Thomas, Y., Jouet, G., Rabineau, M., Droz, L., 2020. Morphology of retrogressive failures in the Eastern Rhone interfluve during the last glacial maximum (Gulf of Lions, Western Mediterranean). Geomorphology 351, 106894. https://doi.org/10.1016/j.geomorph.2019.106894

Baeten, N.J., Laberg, J.S., Vanneste, M., Forsberg, C.F., Kvalstad, T.J., Forwick, M., Vorren, T.O., Haflidason, H., 2014. Origin of shallow submarine mass movements and their glide planes. Sedimentological and geotechnical analyses from the continental slope off northern Norway. Journal of Geophysical Research: Earth Surface 119, 2335–2360. https://doi.org/10.1002/2013JF003068

Bard, E., Hamelin, B., Delanghe-Sabatier, D., 2010. Deglacial Meltwater Pulse 1B and Younger Dryas Sea Levels Revisited with Boreholes at Tahiti. Science 327, 1235. http://dx.doi.org/10.1126/science.1180557

Beiersdorf, H., Kudrass, H.-R., von Stackelberg, U., 1980. Placer Deposits of limenite and Zircon on the Zambezi Shelf. Schweizerbart Science Publishers, Stuttgart, Germany.

Bergh, E.W., von Koslowski, R., Compton, J.S., 2021. Variations in deep water masses along the western margin of South Africa, spanning the last two glacial terminations. Palaeogeography, Palaeoclimatology, Palaeoecology 562, 110148. https://doi.org/10.1016/j.palaeo.2020.110148

Bernhardt, A., Hebbeln, D., Regenberg, M., Lückge, A., Strecker, M.R., 2016. Shelfal sediment transport by an undercurrent forces turbidity-current activity during high sea level along the Chile continental margin. Geology 44, 295–298. https://doi.org/10.1130/G37594.1

Blumsack, S.L., 1993. A model for the growth of mudwaves in the presence of time-varying currents. Deep Sea Research Part II: Topical Studies in Oceanography 40, 963–974. https://doi.org/10.1016/0967-0645(93)90043-M

Blumsack, S.L., Weatherly, G.L., 1989. Observations of the nearby flow and a model for the growth of mudwaves. Deep Sea Research Part A. Oceanographic Research Papers 36, 1327–1339. https://doi.org/10.1016/0198-0149(89)90086-1

Bonnel, C., Dennielou, B., Berné, S., Mulder, T., Droz, L., 2005. Architecture and depositional pattern of the Rhône Neofan and recent gravity activity in the Gulf of Lions (Western Mediterranean). Mar. Pet. Geol. 22, 827–843. https://doi.org/10.1016/j.marpetgeo.2005.03.003

Bourillet, J.-F., Damy, G., Dussud, L., Sultan, N., Woerther, P., Migeon, S., 2007. Behaviour of a piston corer from accelerometers and new insights on quality of the recovery. Presented at the 6th International Off shore Site Investigation and Geotechnics Conference: Confronting New Challenges and Sharing Knowledge, Society of Underwater Technology, SUT, pp. 127–132. https://archimer.ifremer.fr/doc/00071/18198/

Bourillet, J.-F., Ferry, J.-N., Bourges, P., 2013. PAMELA : PASSIVE MARGINS EXPLORATION LABORATORIES [WWW Document]. URL https://doi.org/10.18142/236

Boyd, R., Ruming, K., Goodwin, I., Sandstrom, M., Schröder-Adams, C., 2008. Highstand transport of coastal sand to the deep ocean: A case study from Fraser Island, southeast Australia. Geology 36, 15–18. http://dx.doi.org/10.1130/G24211A.1

Breitzke, M., Wiles, E., Krocker, R., Watkeys, M.K., Jokat, W., 2017. Seafloor morphology in the Mozambique Channel: evidence for long-term persistent bottom-current flow and deep-reaching eddy activity. Marine Geophysical Research 38, 241–269. https://doi.org/10.1007/s11001-017-9322-7

Carvajal, C., Paull, C.K., Caress, D.W., Fildani, A., Lundsten, E., Anderson, K., Maier, K.L., McGann, M., Gwiazda, R., Herguera, J.C., 2017. Unraveling the Channel-Lobe Transition Zone With High-Resolution AUV Bathymetry: Navy Fan, Offshore Baja California, Mexico. J. Sediment. Res. 87, 1049–1059. https://doi.org/10.2110/jsr.2017.58

Castelino, J.A., Reichert, C., Klingelhoefer, F., Aslanian, D., Jokat, W., 2015. Mesozoic and Early Cenozoic sediment influx and morphology of the Mozambique Basin. Mar. Pet. Geol. 66, 890–905. https://doi.org/10.1016/j.marpetgeo.2015.07.028

Cattaneo, A., Correggiari, A., Langone, L., Trincardi, F., 2003. The late-Holocene Gargano subaqueous delta, Adriatic shelf: Sediment pathways and supply fluctuations. Mar. Geol. 193, 61–91. https://doi.org/10.1016/S0025-3227(02)00614-X

Cattaneo, A., Riboulot, V., Jouet, G., Lempereur, C., Scalabrin, C., Marsset T, Le Roy, P., Droz, L., Deville, E., Imbert, P., Contet, J., 2019. Submarine landslides offshore the Zambezi delta and the role of fluids and bottom currents in seafloor detabilization. Presented at the EGU General Assembly, Vienna (Austria).

Clare, M.A., Talling, P.J., Challenor, P., Malgesini, G., Hunt, J., 2014. Distal turbidites reveal a common distribution for large (>0.1 km^3) submarine landslide recurrence. Geology 42, 263–266. https://doi.org/10.1130/G35160.1

Constantinescu, A.M., Toucanne, S., Dennielou, B., Jorry, S.J., Mulder, T., Lericolais, G., 2015. Evolution of the danube deep-sea fan since the last glacial maximum: New insights into Black Sea water-level fluctuations. Mar. Geol. 367, 50–68. http://dx.doi.org/10.1016/j.margeo.2015.05.007

Covault, J.A., Normark, W.R., Romans, B.W., Graham, S.A., 2007. Highstand fans in the California borderland: the overlooked deep-water depositional systems. Geology 35, 783–786. https://doi.org/10.1130/G23800A.1

Curray, J.R., 2014. 50th anniversary commentary. Marine Geology, 50th Anniversary Special Issue 352, 2–3. https://doi.org/10.1016/j.margeo.2014.02.008

de Castro, S., Miramontes, E., Dorador, J., Jouet, G., Cattaneo, A., Rodríguez-Tovar, F.J., Hernández-Molina, F.J., 2021. Siliciclastic and bioclastic contouritic sands: Textural and geochemical characterisation. Marine and Petroleum Geology 128, 105002. https://doi.org/10.1016/j.marpetgeo.2021.105002

de Ruijter, W.P.M., Ridderinkhof, H., Lutjeharms, J.R.E., Schouten, M.W., Veth, C., 2002. Observations of the flow in the Mozambique Channel. Geophysical Research Letters 29, 140-1-140–3. https://doi.org/10.1029/2001GL013714

Dennielou, B., Jallet, L., Sultan, N., Jouet, G., Giresse, P., Voisset, M., Berné, S., 2009. Post-glacial persistence of turbiditic activity within the Rhône deep-sea turbidite system (Gulf of Lions, Western Mediterranean): Linking the outer shelf and the basin sedimentary records. Mar. Geol. 257, 65–86. http://dx.doi.org/10.1016/j.margeo.2008.10.013

Dennielou, B., Jégou, I., Droz, L., Jouet, G., Cattaneo, A., Berné, S., Aslanian, D., Loubrieu, B., Rabineau, M., Bermell, S., 2019. Major modification of sediment routing by a large

Mass Transport Deposit in the Gulf of Lions (Western Mediterranean). Mar. Geol. 411, 1–20. https://doi.org/10.1016/j.margeo.2019.01.011

Deville, E., Marsset, T., Courgeon, S., Jatiault, R., Ponte, J.-P., Thereau, E., Jouet, G., Jorry, S.J., Droz, L., 2018. Active fault system across the oceanic lithosphere of the Mozambique Channel: Implications for the Nubia–Somalia southern plate boundary. Earth and Planetary Science Letters 502, 210–220. https://doi.org/10.1016/j.epsl.2018.08.052

Deville, E., Scalabrin, C., Jouet, G., Cattaneo, A., Battani, A., Noirez, S., Vermesse, H., Olu, K., Corbari, L., Boulard, M., Marsset, T., Dall'Asta, M., Torelli, M., Pastor, L., Pierre, D., Loubrieu, B., 2020. Fluid seepage associated with slope destabilization along the Zambezi margin (Mozambique). Mar. Geol. 428, 106275. https://doi.org/10.1016/j.margeo.2020.106275

Dorschel, B., Jensen, L., Arndt, J.E., Brummer, G.J., de Haas, H., Fielies, A., Franke, D., Jokat, W., Krocker, R., Kroon, D., Pätzold, J., Schneider, R.R., Spieß V, Stollhofen, H., Uenzelmann-Neben, G., Watkeys, M., Wiles, E., 2018. The Southwest Indian Ocean Bathymetric Compilation (swIOBC). Geochemistry, Geophysics, Geosystems 19, 968–976. https://doi.org/10.1002/2017gc007274

Dottore Stagna, M., Maselli, V., Grujic, D., Reynolds, P., Reynolds, D., Iacopini, D., Richards, B., Underhill, J.R., Kroon, D., 2022. Structural controls on slope evolution and sediment dispersal pathways along the northern Tanzania continental margin, western Indian Ocean. Marine Geology 443, 106662. https://doi.org/10.1016/j.margeo.2021.106662

Droz, L., Mougenot, D., 1987. Mozambique Upper Fan: Origin of Depositional Units1. AAPG Bulletin 71, 1355–1365. https://doi.org/10.1306/703C8079-1707-11D7-8645000102C1865D

Dugan, B., 2012. Petrophysical and consolidation behavior of mass transport deposits from the northern Gulf of Mexico, IODP Expedition 308. Mar. Geol. 315–318, 98–107. https://doi.org/10.1016/j.margeo.2012.05.001

Fan, W., McGuire, J.J., Shearer, P.M., 2020. Abundant Spontaneous and Dynamically Triggered Submarine Landslides in the Gulf of Mexico. Geophysical Research Letters 47, e2020GL087213. https://doi.org/10.1029/2020GL087213

Fierens, R., 2019. The Oligocene to Quaternary Zambezi Depositional System (Mozambique Channel, Southwest Indan Ocean): architecture, sedimentation and forcing factors (Doctoral Thesis). Univesité de Bretagne Occidentale, Brest.

Fierens, R., Droz, L., Jouet, G., Rabineau, M., Raisson, F., Babonneau, N., Robin, C., Jorry, S.J., 2022. Sedimentary evolution and effects of structural controls on the development of the Zambezi mixed turbidite-contourite system (Mozambique Channel, Southwest Indian Ocean) since the Oligocene. Marine and Petroleum Geology 138, 105532. https://doi.org/10.1016/j.marpetgeo.2022.105532

Fierens, R., Droz, L., Toucanne, S., Raisson, F., Jouet, G., Babonneau, N., Miramontes, E., Landurain, S., Jorry, S.J., 2019. Late Quaternary geomorphology and sedimentary processes in the Zambezi turbidite system (Mozambique Channel). Geomorphology 334, 1–28. https://doi.org/10.1016/j.geomorph.2019.02.033

Fierens, R., Toucanne, S., Droz, L., Jouet, G., Raisson, F., Jorissen, E.L., Bayon, G., Giraudeau, J., Jorry, S.J., 2020. Quaternary sediment dispersal in the Zambezi turbidite system (SW Indian Ocean). Marine Geology 428, 106276. https://doi.org/10.1016/j.margeo.2020.106276

Flemming, B.W., Kudrass, H.-R., 2018. Large dunes on the outer shelf off the Zambezi Delta, Mozambique: evidence for the existence of a Mozambique Current. Geo-Mar. Lett. 38, 95–106. https://doi.org/10.1007/s00367-017-0515-5

Flood, R.D., 1988. A lee wave model for deep-sea mudwave activity. Deep-Sea Research 973–983. https://doi.org/10.1016/0198-0149(88)90071-4

Franke, D., Bargeloh, H.-O., Behrens, T., Berglar, K., Chaheire, M., Damm, V., Demir, U., Ebert, T., Ehrhardt, A., Engels, M., Goldmann, F., Kallaus, G., Kaufmann, D., Klimke, J., Ladage, S., Lutz, R., Ponte, J.-P., Schnabel, M., Schrader, U., Schreckenberger, B., Slabon, P., Stollhofen, H., 2014. Der passive und der gescherte Kontinentrand vor Mosambik: Früher Zerfall Gondwanas und der rezente Einfluss des ostafrikanischen Riftsystems (The passive and rifted continental margin off Mozambique: Early dispersal of Gondwana and the recent influence of the East African rift system) (PAGE-Four), Report of RV "Sonne" cruise SO-231, Project PAGE-Four, 20. February 2014 to 29. March 2014. Hannover.

Franke, D., Jokat, W., Ladage, S., Stollhofen, H., Klimke, J., Lutz, R., Mahanjane, E.S., Ehrhardt, A., Schreckenberger, B., 2015. The offshore East African Rift System: Structural framework at the toe of a juvenile rift. Tectonics 34, 2086–2104. https://doi.org/10.1002/2015TC003922

Gaudin, M., Berné, S., Jouanneau, J.-M., Palanques, A., Puig, P., Mulder, T., Cirac, P., Rabineau, M., Imbert, P., 2006. Massive sand beds attributed to deposition by dense water cascades in the Bourcart canyon head, Gulf of Lions (northwestern Mediterranean Sea). Marine Geology, EUROSTRATAFORM VOL. 1: Source to Sink Sedimentation on the European Margin 234, 111–128. https://doi.org/10.1016/j.margeo.2006.09.020

GEBCO, 2014. GEBCO_2014 Grid. British Oceanographic Data Centre (BODC) [WWW Document]. GEBCO_2014 Grid. British Oceanographic Data Centre (BODC). URL http://www.gebco.net/data_and_products/gridded_bathymetry_data/

Grimison, N.L., Chen, W.-P., 1988. Earthquakes in the Davie Ridge-Madagascar region and the southern Nubian-Somalian plate boundary. Journal of Geophysical Research: Solid Earth 93, 10439–10450. https://doi.org/10.1029/JB093iB09p10439

Haflidason, H., Sejrup, H.P., Nygård, A., Mienert, J., Bryn, P., Lien, R., Forsberg, C.F., Berg, K., Masson, D., 2004. The Storegga Slide: architecture, geometry and slide development. Mar. Geol. 213, 201–234. http://dx.doi.org/10.1016/j.margeo.2004.10.007

Hanebuth, T.J.J., Lantzsch, H., Nizou, J., 2015. Mud depocenters on continental shelves,Äîappearance, initiation times, and growth dynamics. Geo-Mar. Lett. 35, 487–503. https://doi.org/10.1007/s00367-015-0422-6

Heaton, T.J., Köhler, P., Butzin, M., Bard, E., Reimer, R.W., Austin, W.E.N., Ramsey, C.B., Grootes, P.M., Hughen, K.A., Kromer, B., Reimer, P.J., Adkins, J., Burke, A., Cook, M.S., Olsen, J., Skinner, L.C., 2020. Marine20—The Marine Radiocarbon Age Calibration Curve (0–55,000 cal BP). Radiocarbon 62, 779–820. https://doi.org/10.1017/RDC.2020.68

Jokat, W., 2014. The Expedition of the Research Vessel "Sonne" to the Mozambique Basin in 2014 (SO-230), Berichte zur Polar- und Meeresforschung = Reports on Polar and Marine Research. Bremerhaven, Germany.

Jouet, G., Deville, E., 2015. PAMELA-MOZ04 cruise, RV Pourquoi pas ? [WWW Document]. URL https://doi.org/10.17600/15000700

Kolla, V., Kostecki, J.A., Henderson, L., Hess, L., 1980. Morphology and Quaternary sedimentation of the Mozambique Fan and environs, southwestern Indian Oceans*. Sedimentology 27, 357–378. https://doi.org/10.1111/j.1365-3091.1980.tb01188.x

Kongsberg Maritime AS, 2011. Kongsberg EM122 Multibeam Echo Sounder - Product Description [WWW Document]. EPIC3Kongsberg Maritime AS, Ref. E, 56 p. URL https://epic.awi.de/id/eprint/45364/ (accessed 8.6.22).

Laberg, J.S., Camerlenghi, A., 2008. Chapter 25 The Significance of Contourites for Submarine Slope Stability, in: Rebesco, M., Camerlenghi, A. (Eds.), Developments in Sedimentology, Contourites. Elsevier, pp. 537–556. https://doi.org/10.1016/S0070-4571(08)10025-5

Lemoine, F., 1998. Changements de l'hydrologie de surface (temperature et salinite) de l'ocean austral en relation avec les variations de la circulation thermohaline au cours des deux derniers cycles climatiques (These de doctorat). Paris 6.

Li, W., Alves, T.M., Urlaub, M., Georgiopoulou, A., Klaucke, I., Wynn, R.B., Gross, F., Meyer, M., Repschläger, J., Berndt, C., Krastel, S., 2017. Morphology, age and sediment dynamics of the upper headwall of the Sahara Slide Complex, Northwest Africa: Evidence for a large Late Holocene failure. Mar. Geol. 393, 109–123. https://doi.org/10.1016/j.margeo.2016.11.013

Maboya, M.L., Meadows, M.E., Reimer, P.J., Backeberg, B.C., Haberzettl, T., 2018. Late Holocene Marine Radiocarbon Reservoir Correction for the Southern and Eastern Coasts of South Africa. Radiocarbon 60, 571–582. https://doi.org/10.1017/RDC.2017.139

Macdonald, H.A., Wynn, R.B., Huvenne, V.A.I., Peakall, J., Masson, D.G., Weaver, P.P.E., McPhail, S.D., 2011. New insights into the morphology, fill, and remarkable longevity (>0.2 m.y.) of modern deep-water erosional scours along the northeast Atlantic margin. Geosphere 7, 845–867. https://doi.org/10.1130/ges00611.1

Maselli, V., Iacopini, D., Ebinger, C.J., Tewari, S., de Haas, H., Wade, B.S., Pearson, P.N., Francis, M., van Vliet, A., Richards, B., Kroon, D., 2020a. Large-scale mass wasting in the western Indian Ocean constrains onset of East African rifting. Nat Commun 11, 3456. https://doi.org/10.1038/s41467-020-17267-5

Maselli, V., Kroon, D., Iacopini, D., Wade, B.S., Pearson, P.N., de Haas, H., 2020b. Impact of the East African Rift System on the routing of the deep-water drainage network offshore Tanzania, western Indian Ocean. Basin Research 32, 789–803. https://doi.org/10.1111/bre.12398

Masson, D.G., Harbitz, C.B., Wynn, R.B., Pedersen, G., Løvholt, F., 2006. Submarine landslides: processes, triggers and hazard prediction. Philosophical Transactions of the Royal Society A: Mathematical, Physical and Engineering Sciences 364, 2009–2039. https://doi.org/10.1098/rsta.2006.1810

Mazières, A., Gillet, H., Castelle, B., Mulder, T., Guyot, C., Garlan, T., Mallet, C., 2014. High-resolution morphobathymetric analysis and evolution of Capbreton submarine canyon head (Southeast Bay of Biscay—French Atlantic Coast) over the last decade using descriptive and numerical modeling. Mar. Geol. 351, 1–12. https://doi.org/10.1016/j.margeo.2014.03.001

McCave, I.N., 2017. Formation of sediment waves by turbidity currents and geostrophic flows: A discussion. Marine Geology 390, 89–93. https://doi.org/10.1016/j.margeo.2017.05.003

Meiburg, E., Kneller, B., 2010. Turbidity Currents and Their Deposits. Annu. Rev. Fluid Mech. 42, 135–156. https://doi.org/10.1146/annurev-fluid-121108-145618

Milliman, J.D., Meade, R.H., 1983. World-wide delivery of river sediment to the oceans. J. Geol. 41–55. https://www.jstor.org/stable/30060512

Miramontes, E., Garziglia, S., Sultan, N., Jouet, G., Cattaneo, A., 2018. Morphological control of slope instability in contourites: a geotechnical approach. Landslides 15, 1085–1095. https://doi.org/10.1007/s10346-018-0956-6

Miramontes, E., Jorry, S.J., Jouet, G., Counts, J.W., Courgeon, S., Le Roy, P., Guerin, C., Hernández-Molina, F.J., 2019a. Deep-water dunes on drowned isolated carbonate terraces (Mozambique Channel, south-west Indian Ocean). Sedimentology 66, 1222–1242. https://doi.org/10.1111/sed.12572

Miramontes, E., Jouet, G., Thereau, E., Bruno, M., Penven, P., Guerin, C., Le Roy, P., Droz, L., Jorry, S.J., Hernandez-Molina, F.J., Thiéblemont, A., Silva Jacinto, R., Cattaneo, A., 2020. The impact of internal waves on upper continental slopes: insights from the Mozambican margin (southwest Indian Ocean). Earth Surface Processes and Landforms. https://doi.org/10.1002/esp.4818

Miramontes, E., Penven, P., Fierens, R., Droz, L., Toucanne, S., Jorry, S.J., Jouet, G., Pastor, L., Silva Jacinto, R., Gaillot, A., Giraudeau, J., Raisson, F., 2019b. The influence of bottom currents on the Zambezi Valley morphology (Mozambique Channel, SW Indian Ocean): In situ current observations and hydrodynamic modelling. Mar. Geol. 410, 42–55. https://doi.org/10.1016/j.margeo.2019.01.002

Miramontes, E., Thiéblemont, A., Babonneau, N., Penven, P., Raisson, F., Droz, L., Jorry, S.J., Fierens, R., Counts, J.W., Wilckens, H., Cattaneo, A., Jouet, G., 2021. Contourite and mixed turbidite-contourite systems in the Mozambique Channel (SW Indian Ocean): Link between geometry, sediment characteristics and modelled bottom currents. Marine Geology 437, 106502. https://doi.org/10.1016/j.margeo.2021.106502

Nittrouer, C., Kravitz, J., 1996. STRATAFORM: A Program to Study the Creation and Interpretation of Sedimentary Strata on Continental Margins. oceanog 9, 146–152. https://doi.org/10.5670/oceanog.1996.01

Normandeau, A., Lajeunesse, P., St-Onge, G., 2013. Shallow-water longshore drift-fed submarine fan deposition (Moisie River Delta, Eastern Canada). Geo-Mar. Lett. 33, 391–403. https://doi.org/10.1007/s00367-013-0336-0

Ortiz, A., Rabineau, M., Robin, C., Jouet, G., Dall'Asta, M., 2016. Analyse sismo-stratigraphique des sériespléistocènes de la plate-forme duMozambique, in: 25 Ème Réunion Des Sciences de La Terre (RST 2016). Société Géologique de France, Caen, France, p. 248.

Patruno, S., Hampson, G.J., Jackson, C.A.L., 2015. Quantitative characterisation of deltaic and subaqueous clinoforms. Earth-Science Reviews 142, 79–119. https://doi.org/10.1016/j.earscirev.2015.01.004

Payton, C.E., 1977. Seismic Stratigraphy—Applications to Hydrocarbon Exploration, AAPG Special Publications. Tulsa.

Penven, P., Lutjeharms, J.R.E., Florenchie, P., 2006. Madagascar: A pacemaker for the Agulhas Current system? Geophysical Research Letters 33. https://doi.org/10.1029/2006GL026854

Piper, D.J.W., Cochonat, P., Morrison, M.L., 1999. The sequence of events around the epicentre of the 1929 Grand Banks earthquake: initiation of debris flows and turbidity current inferred from sidescan sonar. Sedimentology 46, 79–97. https://doi.org/10.1046/j.1365-3091.1999.00204.x

Pohl, F., Eggenhuisen, J.T., Cartigny, M.J.B., Tilston, M.C., de Leeuw, J., Hermidas, N., 2020. The influence of a slope break on turbidite deposits: An experimental

investigation. Mar. Geol. 424, 106160. https://doi.org/10.1016/j.margeo.2020.106160

Pohl, F., Eggenhuisen, J.T., Tilston, M., Cartigny, M.J.B., 2019. New flow relaxation mechanism explains scour fields at the end of submarine channels. Nat. Commun. 10, 4425. https://doi.org/10.1038/s41467-019-12389-x

Poncelet, C., Billant, G., Corre, M.-P., 2020. Globe (GLobal Oceanographic Bathymetry Explorer) Software.

Ponte, J.-P., Robin, C., Guillocheau, F., Popescu, S., Suc, J.-P., Dall,ÄôAsta, M., Melinte-Dobrinescu, M.C., Bubik, M., Dupont, G., Gaillot, J., 2019. The Zambezi delta (Mozambique channel, East Africa): High resolution dating combining bio- orbital and seismic stratigraphies to determine climate (palaeoprecipitation) and tectonic controls on a passive margin. Mar. Pet. Geol. 105, 293–312. https://doi.org/10.1016/j.marpetgeo.2018.07.017

Rabineau, M., Berne, S., Aslanian, D., Olivet, J.-L., Joseph, P., Guillocheau, F., Bourillet, J.-F., Ledrezen, E., Granjeon, D., 2005. Sedimentary sequences in the Gulf of Lion: A record of 100,000 years climatic cycles. Mar. Pet. Geol. 22, 775–804. https://doi.org/10.1016/j.marpetgeo.2005.03.010

Rabineau, M., Berné, S., Ledrezen, É., Lericolais, G., Marsset, T., Rotunno, M., 1998. 3D architecture of lowstand and transgressive Quaternary sand bodies on the outer shelf of the Gulf of Lion, France. Marine and Petroleum Geology 15, 439–452. https://doi.org/10.1016/S0264-8172(98)00015-4

Raillard, S., 1990. Les marges de l'Afrique de l'Est et les zones de fractures associées : chaîne Davie et ride du Mozambique (PhD Thesis). Université Paris VI, Paris, France.

Raisson, F., Cazzola, C., Ferry, J.-N., 2016. Deep oceanic currents and sea floor interactions offshore SE Africa. Presented at the the EGU General Assembly Conference Abstracts, Vienna (Austria).

Rebesco, M., Hernández-Molina, F.J., Van Rooij, D., Wåhlin, A., 2014. Contourites and associated sediments controlled by deep-water circulation processes: State-of-the-art and future considerations. Mar. Geol. 352, 111–154. https://doi.org/10.1016/j.margeo.2014.03.011

Reeves, J.M., Chivas, A.R., Garcia, A., Holt, S., Couapel, M.J.J., Jones, B.G., Cendón, D.I., Fink, D., 2008. The sedimentary record of palaeoenvironments and sea-level change in the Gulf of Carpentaria, Australia, through the last glacial cycle. Quaternary International, Subaerially exposed continental shelves: contributions from INQUA Project 0419 183, 3–22. https://doi.org/10.1016/j.quaint.2007.11.019

Reichert, C., Aslanian, D., 2007. MD 163 / MOBAMASIS cruise, RV Marion Dufresne [WWW Document]. URL https://doi.org/10.17600/7200110

Richter, T.O., Van der Gaast, S.J., Koster, B., Vaars, A.J., Gieles, R., De Stigter, H.C., De Haas, H., Van Weering, T.C.E., 2006. The Avaatech XRF Core Scanner: technical description and applications to NE Atlantic sediments, in: Rothwell, R.G. (Ed.), New Techniques in Sediment Core Analysis, Special Publications. Geological Society, London, pp. 39–50.

Ridderinkhof, H., de Ruijter, W.P.M., 2003. Moored current observations in the Mozambique Channel. Deep Sea Research Part II: Topical Studies in Oceanography 50, 1933–1955. https://doi.org/10.1016/S0967-0645(03)00041-9

Rothwell, R.G., 2006. New Techniques in Sediment Core Analysis, Special Publications. Geological Society, London.

Sætre, R., Da Silva, A.J., 1984. The circulation of the Mozambique channel. Deep Sea Research Part A. Oceanographic Research Papers 31, 485–508. https://doi.org/10.1016/0198-0149(84)90098-0

Schefuß, E., Kuhlmann, H., Mollenhauer, G., Prange, M., Pätzold, J., 2011. Forcing of wet phases in southeast Africa over the past 17,000 years. Nature 480, 509–512. https://doi.org/10.1038/nature10685

Schouten, M.W., de Ruijter, W.P.M., van Leeuwen, P.J., Ridderinkhof, H., 2003. Eddies and variability in the Mozambique Channel. Deep Sea Research Part II: Topical Studies in Oceanography 50, 1987–2003. https://doi.org/10.1016/S0967-0645(03)00042-0

Schulz, H., Lückge, A., Emeis, K.-C., Mackensen, A., 2011. Variability of Holocene to Late Pleistocene Zambezi riverine sedimentation at the upper continental slope off Mozambique, 15°—21°S. Mar. Geol. 286, 21–34. https://doi.org/10.1016/j.margeo.2011.05.003

Siddorn, J.R., Bowers, D.G., Hoguane, A.M., 2001. Detecting the Zambezi River Plume using Observed Optical Properties. Marine Pollution Bulletin 42, 942–950. https://doi.org/10.1016/S0025-326X(01)00053-4

Sierro, F.J., Andersen, N., Bassetti, M.A., BernÈ, S., Canals, M., Curtis, J.H., Dennielou, B., Flores, J.A., Frigola, J., Gonzalez-Mora, B., Grimalt, J.O., Hodell, D.A., Jouet, G., PÈrez-Folgado, M., Schneider, R., 2009. Phase relationship between sea level and abrupt climate change. Quat. Sci. Rev. 28, 2867–2881. https://doi.org/10.1016/j.quascirev.2009.07.019

Simmons, M.D., 2012. Chapter 13 - Sequence Stratigraphy and Sea-Level Change, in: Gradstein, F.M., Ogg, J.G., Schmitz, M.D., Ogg, G.M. (Eds.), The Geologic Time Scale. Elsevier, Boston, pp. 239–267. https://doi.org/10.1016/B978-0-444-59425-9.00013-5

Smith, D.E., Harrison, S., Jordan, J.T., 2013. Sea level rise and submarine mass failures on open continental margins. Quaternary Science Reviews 82, 93–103. https://doi.org/10.1016/j.quascirev.2013.10.012

Southon, J., Kashgarian, M., Fontugne, M., Metivier, B., Yim, W.W.-S., 2002. Marine Reservoir Corrections for the Indian Ocean and Southeast Asia. Radiocarbon 44, 167–180. https://doi.org/10.1017/S0033822200064778

Stoecklin, A., Friedli, B., Puzrin, A.M., 2017. Sedimentation as a Control for Large Submarine Landslides: Mechanical Modeling and Analysis of the Santa Barbara Basin. Journal of Geophysical Research: Solid Earth 122, 8645–8663.

Stow, D.A.V., Piper, D.J.W., 1984. Deep-water fine-grained sediments: facies models, in: Stow, D.A.V., Piper, D.J. (Eds.), Fine-Grained Sediments: Deep-Water Processes and Facies. Blackwell Scientific Publications, pp. 611–646.

Stuiver, M., Reimer, P.J., Reimer, R.W., 2018. CALIB 7.1 [WWW program] [WWW Document].

Sultan, N., Cochonat, P., Canals, M., Cattaneo, A., Dennielou, B., Haflidason, H., Laberg, J.S., Long, D., Mienert, J., Trincardi, F., 2004. Triggering mechanisms of slope instability processes and sediment failures on continental margins: a geotechnical approach. Mar. Geol. 213, 291–321. https://doi.org/10.1016/j.margeo.2004.10.011

Symons, W.O., Sumner, E.J., Talling, P.J., Cartigny, M.J.B., Clare, M.A., 2016. Large-scale sediment waves and scours on the modern seafloor and their implications for the prevalence of supercritical flows. Mar. Geol. 371, 130–148. https://doi.org/10.1016/j.margeo.2015.11.009

Talling, P.J., Clare, M.A., Urlaub, M., Pope, E.L., Hunt, J.E., Watt, S.F.L., 2014. Large Submarine Landslides on Continental Slopes: Geohazards, Methane Release, and Climate Change. Oceanography 27, 32–45.

Ternon, J.F., Roberts, M.J., Morris, T., Hancke, L., Backeberg, B., 2014. In situ measured current structures of the eddy field in the Mozambique Channel. Deep Sea Research Part II: Topical Studies in Oceanography 100, 10–26. https://doi.org/10.1016/j.dsr2.2013.10.013

Thiéblemont, A., Hernández-Molina, F.J., Miramontes, E., Raisson, F., Penven, P., 2019. Contourite depositional systems along the Mozambique channel: The interplay between bottom currents and sedimentary processes. Deep Sea Research Part I: Oceanographic Research Papers 147, 79–99. https://doi.org/10.1016/j.dsr.2019.03.012

Thompson, J.O., 2017. The opening of the Indian Ocean: what is the impact on the East African, Madagascar and Antarctic margins, and what are the origins of the aseismic ridges? (PhD Thesis). Université de Rennes 1, France.

Trincardi, F., Cattaneo, A., Correggiari, A., Mongardi, S., Breda, A., Asioli, A., 2003. Submarine Slides During Relative Sea Level Rise: Two Examples from the Eastern Tyrrhenian Margin, in: Locat, J., Mienert, J., Boisvert, L. (Eds.), Submarine Mass Movements and Their Consequences: 1st International Symposium, Advances in Natural and Technological Hazards Research. Springer Netherlands, Dordrecht, pp. 469–478. https://doi.org/10.1007/978-94-010-0093-2_52

Ullgren, J.E., André, E., Gammelsrød, T., Hoguane, A.M., 2016. Observations of strong ocean current events offshore Pemba, Northern Mozambique. Journal of Operational Oceanography 9, 55–66. https://doi.org/10.1080/1755876X.2016.1204172

Ullgren, J.E., van Aken, H.M., Ridderinkhof, H., de Ruijter, W.P.M., 2012. The hydrography of the Mozambique Channel from six years of continuous temperature, salinity, and velocity observations. Deep Sea Research Part I: Oceanographic Research Papers 69, 36–50. https://doi.org/10.1016/j.dsr.2012.07.003

Urlaub, M., Talling, P.J., Masson, D.G., 2013. Timing and frequency of large submarine landslides: implications for understanding triggers and future geohazard. Quat. Sci. Rev. 72, 63–82. https://doi.org/10.1016/j.quascirev.2013.04.020

Vail, P.R., Mitchum, R.M., Todd, R.G., Widmier, J.M., Thompson III, S., Sangree, J.B., Bubb, J.N., Hatelid, W.G., 1977. Seismic stratigraphy and global changes of sea level, in: Payton, C.E. (Ed.) Seismic Stratigraphy—Applications to Hydrocarbon Exploration, American Association of Petroleum Geologists Memoir. pp. 49–212.

Van Campo, E., Duplessy, J.C., Prell, W.L., Barratt, N., Sabatier, R., 1990. Comparison of terrestrial and marine temperature estimates for the past 135 kyr off southeast Africa: a test for GCM simulations of palaeoclimate. Nature 348, 209–212. https://doi.org/10.1038/348209a0

van der Lubbe, H.J.L., Frank, M., Tjallingii, R., Schneider, R.R., 2016. Neodymium isotope constraints on provenance, dispersal, and climate-driven supply of Zambezi sediments along the Mozambique Margin during the past ~45,000 years. Geochemistry, Geophysics, Geosystems 17, 181–198. https://doi.org/10.1002/2015GC006080

van der Lubbe, J.J.L., Tjallingii, R., Prins, M.A., Brummer, G.-J.A., Jung, S.J.A., Kroon, D., Schneider, R.R., 2014. Sedimentation patterns off the Zambezi River over the last 20,000 years. Mar. Geol. 355, 189–201. http://dx.doi.org/10.1016/j.margeo.2014.05.012

Van Wagoner, J.C., Posamentier, H.W., Mitchum, R.M., Vail, P.R., Sarg, J.F., Loutit, T.S., Hardenbol, J., 1988. An overview of the fundamentals of sequence stratigraphy and key definitions, in: Wilgus, C.K., Hastings, B.S., Kendall, C.G., Posamentier, H.W., Ross, C.A., Van wagoner, J.C. (Eds.), Sea-Level Changes: An Integrated Approach. SEPM Special Publication, Tulsa, pp. 39–45.

Walling, D.E., 1984. The sediment yields of African rivers, in: Walling, D.E., Foster, S.S.D., Wurzel, P. (Eds.), . Presented at the Challenges in African Hydrology and Water Resources (Proceedings of Harare Symposium), IAHS.

Weaver, P.P.E., Canals, M., Trincardi, F., 2006. EUROSTRATAFORM Special Issue of Marine Geology. Mar. Geol. 234, 1–2.

Wiles, E., Green, A.N., Watkeys, M.K., Jokat, W., 2017. Zambezi continental margin: compartmentalized sediment transfer routes to the abyssal Mozambique Channel. Marine Geophysical Research 38, 227–240. https://doi.org/10.1007/s11001-016-9301-4

Wynn, R.B., Kenyon, N.H., Masson, D.G., Stow, D.A.V., Weaver, P.P.E., 2002. Characterization and recognition of deep-water channel-lobe transition zones. Am. Assoc. Pet. Geol. Bull. 86, 1441–146. http://dx.doi.org/10.1306/61EEDCC4-173E-11D7-8645000102C1865D

Zindorf, M., Rooze, J., Meile, C., März, C., Jouet, G., Newton, R., Brandily, C., Pastor, L., 2021. The evolution of early diagenetic processes at the Mozambique margin during the last glacial-interglacial transition. Geochimica et Cosmochimica Acta 300, 79–94. https://doi.org/10.1016/j.gca.2021.02.024

Figures caption

Figure 1

Bathymetric map of the Mozambique Channel showing the oceanic circulation (AABW: Antarctic Bottom Water, AAIW: Antarctic Intermediate Water, NADW: North Atlantic Deep Water, MUC: Mozambique Under Current, MC: Mozambique Current), location of earthquakes (NEIC catalogue, USGS), area with active faults at the Western East African Rift System (red dash line) (Deville et al. 2018).

Figure 2

Study area with identification of main morphological and sedimentary features on the Zambezi/Mozambique margin. Location of sediment cores. See location of the north-east area (indicated as Figure 3) and south-west area (indicated in Fig. 11). The continental

shelf is indicated in light blue; black dotted line indicates the shelf edge around 80-100 m (GEBCO, 2014). (1) Dune field is after (Flemming and Kudrass, 2018; Miramontes et al., 2020); (2) Mud belts from (Beiersdorf et al., 1980; Schulz et al., 2011); (3) Contouritic deposits adapted from (Fierens et al., 2019) after (Raillard, 1990; Raisson et al., 2016; Thompson, 2017; Wiles et al., 2017); (4) after (Fierens et al., 2019; Wiles et al., 2017). Inset: bottom circulation (blue arrows) and coastal surface circulation (black arrows) after (Miramontes et al., 2019b; Sætre and Da Silva, 1984), MC: Mozambique Current, MUC: Mozambique Under Current.

Figure 3

Multibeam data and location of sediment cores on the north-east upper slope (see location in Fig. 2). Black dotted line indicates the shelf break around 80-100 m and grey shading indicates seabed slopes from GEBCO (2014). Blue lines outline canyons (C) and gullies (G). Bathymetry: PAMELA project (IFREMER and TotalEnergies) and courtesy of the Alfred Wegener Institut, Hemholtz Centre for Polar and Marine Research.

Figure 4

Zoom on the north-east upper slope showing canyons, gullies and multiple head scars (see location in Fig. 3). Black dotted line indicates the shelf break around 80-100 m and grey shading indicates seabed slopes from GEBCO (2014). Bathymetry: PAMELA project (IFREMER and TotalEnergies) and courtesy of the Alfred Wegener Institut, Hemholtz Centre for Polar and Marine Research.

Figure 5

(A) Sub-bottom profiler strike line and seabed morphology on the northeast upper slope; (B and C) zoom in: yellow indicates transparent seismic facies interpreted as mass-transport deposits, blue indicates stratified deposits corresponding to the Holocene sediment wedge (cf. Fig. 7); (B) slight undulations in stratified deposits topped by transparent deposits; (C) stratified deposits pinching out away from the canyon, yellow corresponds to TL1ne identified on the SBP dip line (Fig. 7).

Figure 6

(A) Sub-bottom profiler line and seabed morphology on the north-east mid- and base of slope (see location on Fig. 3); (B and C) zoom: yellow indicates transparent seismic facies, either TL1ne or TL2ne interpreted as mass transport deposits; (B) morphological interaction between canyons and sediment waves; (C) trains of sediment waves with upslope increasing wave length.

Figure 7

(A) Sub-bottom profiler line along the north-east slope (see location on Fig. 4); (B) zoom on mid-slope showing the superposition of transparent facies (TL1ne in yellow) and stratified facies (SL1ne and SL2ne in blue and red) corresponding to the distal part of the Late Holocene sediment wedge on the upper slope; (C) Late Holocene sediment wedge deposited on the upper slope (SL1ne and SL2ne in blue and red). See the buried head scarp, sliding and mass transport deposit (yellow) affecting the upper part of the wedge; see location of sediment core MOZ4-CSF13 (cf. Fig. 9).

Figure 8

Sub-bottom profiler line and seabed morphology of base of slope in the north-east area (see location on Fig. 3). See the headscarp and mass transport deposit (TL2ne in yellow). See scours and location of sediment core MOZ4-CSF11 (cf. Fig. 9). Top right, zoom showing the seabed blocky pattern.

Figure 9

Summary lithologic logs of sediment cores, radiocarbon dates, sedimentation rates, median grain size, gamma-density, Log(Ca/Fe), corresponding sub-bottom profiler facies. Depth between parentheses indicate the maximum penetration of the corer and correspond to the maximum depth sampled in the sediment cores

Figure 10

Sub-bottom profiler lines and seabed morphology at the base of slope in north-east area; (A) giant scours (see location of sediment core MOZ4-CSF11); (C) short-wave-length sediment waves. Location and penetration of core MOZ4-CSF11 is indicated with a red line.

Figure 11

(A) Seabed morphology of the south-west area; black dotted line indicates the shelf break around 80-100 m (from GEBCO, 2014); (B) zoom on giant slide scar and headwall on the upper slope; (C) zoom on the upper slope erosive channel (Miramontes et al., 2020) and carbonate reefs. See location of sediment core MOZ4-CSF18.

Figure 12

Sub-bottom profiler lines on the Mozambique upper slope in the south-west area between 19°55S and 19°20S; see location in Fig. 11. (A) Line across the slope and the

slide scar; yellow indicates a transparent facies (TLsw) interpreted as a mass transport deposit; blue indicates the stratified Holocene deposit (SL2sw) in the slide scar. (B) Line along the upper slope adjacent to the slide scar; see the stratified facies; yellow line indicates a prominent high-amplitude reflector (R). (C) Line across the upper slope showing a carbonate reef and a contourite terrace; yellow line, see above. (D) zoom on line C showing from base to top : the stratified layer (SL1sw), the high-amplitude reflector (R) and 2-m-thick high-amplitude interval (HL) and the along-slope erosional channel described in Miramontes et al. (2020).

Figure 13

Morphology of the slide scar on the Mozambique upper slope in the south-west area around 19°50S (see location on Fig. 11A). The area in blue corresponds to Holocene deposits in the slide scar (SL2sw unit); bold numbers indicate the thickness of the deposit in metres; dotted lines represent the location of sub-bottom profiler lines used to map the Holocene deposit. See location of sediment core MOZ4-CSF18.

Figure 14

Sub-bottom profiler line on a slide scar of the Zambezi upper slope in the south-west area around 19°50S; blue indicates the Holocene deposit (SL2sw) in the slide scar; see location in Fig. 13.

Figure 15

Sub-bottom profiler lines on the Mozambique upper slope in the south-west area around 19°20S and correlation with magnetic susceptibility from sediment cores and with the chronostratigraphic framework based on AMS radiocarbon dating (see the age of 27.8

cal ka BP at the base of core MOZ4-CSF17). The dotted yellow line indicates a prominent high amplitude reflector (R) penetrated by the sediment cores. HL = high amplitude interval (cf. Fig. 13). Red vertical lines indicate the position and penetration of sediment cores. See location in Figs 11A and 13C.

Figure 16

Map of the shelf and upper slope of the Zambezi margin showing the extension (blue) of a high-amplitude reflector R identified on sub-bottom profiler lines (cf. Fig. 15). The reflector corresponds to the top of the deposits around the period of the Bolling-Allerod to Younger Dryas climatic instability. The surface in green indicates the extension of the flooded area on the shelf during the Bolling/Allerod to Younger Dryas period (between ca. 80-60 m) and between the Younger Dryas, and the beginning of the Holocene (ca. 40 m). The flooding of the shelf and sediment starvation of the upper slope occurred earlier in the south-east area than in the north west area. Thin dotted lines show the location of sub-bottom profiler lines. Black dotted line indicates the shelf break around 80-100 m (from GEBCO, 2014).

Figure 17

Summary of the patterns of sedimentation from the shelf edge to the base-of-slope on the Mozambique-Zambezi margin (17°30'S-20°S) during the last 40 ka

Tables

Core	Location	Latitude	Longitude	Depth (m)	Recovered length (mbsf)	Penetration (m)	IGSN
MOZ4-CSF11	base of slope	S17° 49.499'	E 039°11.192'	2134	9.70	10,45	http://igsn.org/BFBGX-85854
MOZ4-CSF12	base of slope	S17° 39.309'	E 038°59.002'	1905	8.70	10.20	http://igsn.org/BFBGX-85860
MOZ4-CSF13	mid-slope	S 17°27.832'	E038° 45.270'	904	14.61	15.80	http://igsn.org/BFBGX-85861
MOZ4-CSF18	upper slope	S19° 50.631'	E036° 30.7860’	410	9.41	10,74	http://igsn.org/BFBGX-128003
MOZ4-CSF19	upper slope	S19° 23.399’	E036° 52.3279’	315	9.12	10.38	http://igsn.org/BFBGX-128004

Table 1: Location and characteristics of sediment cores used in this study. Penetration is that of the corer and therefore of the base of the core below seafloor, calculated after corer cinematic data; mbsf = metres below seafloor. IGSN = International Geo Sample Number (hyperlink to webpages with sample metadata).

Core	Depth in core (cm)	Radiocarbon age (yr BP)	2σ calendar age (yr BP) ΔR=45	Median calendar age (yr BP)	Material	Lab. Number
MOZ4-CSF19	5-6	3,170±30	2,481 - 3,023	2,761	G. trilobus trilobus	Beta-447916
MOZ4-CSF19	215-216	8,710±30	8,868 - 9,407	9,135	G. trilobus trilobus	Beta-447917
MOZ4	300-301	10,180±30	10,729 -	11,060	Bulk planktonic	Beta-

- CSF19			11,311		foraminifera	462599
MOZ4 - CSF19	450-451	11,320±30	12,417 - 12,834	12,631	Bulk planktonic foraminifera	Beta-462602
MOZ4 - CSF19	710-711	13,240±40	14,653 - 15,361	15,031	Bulk planktonic foraminifera	Beta-470569
MOZ4 - CSF19	905-906	14,950±50	16,895 - 17,564	17,208	Bulk foraminifera	Beta-447918
MOZ4 - CSF18	2-3	50±30	Modern	Modern	G. trilobus trilobus	Beta-447914
MOZ4 - CSF18	180-181	2,010±30	1,144 - 1,600	1,367	Bulk foraminifera	Beta-470570
MOZ4 - CSF18	550-551	4,600±30	4,294 - 4,826	4,567	Bulk foraminifera	Beta-470571
MOZ4 - CSF18	925-926	6,610±30	6,606 - 7,128	6,847	G. ruber, G. trilobus, G. sacculifer	Beta-447915
MOZ4 - CSF11	30-31	31,470±160	34,571 - 35,409	35,011	G. ruber, G. trilobus, G. sacculifer	Beta-462594
MOZ4 - CSF11	279-280	> 43500	–	–	Bulk foraminifera	Beta-470559
MOZ4 - CSF11	453-454	> 43500	–	–	Bulk foraminifera	Beta-470560
MOZ4 - CSF11	580-581	39,510±530	41,803 - 42,892	42,334	G. ruber, G. trilobus, G. sacculifer	Beta-462593

MOZ4-CSF12	10-11	29,750±30	33,059 - 33,703	33,379	G. ruber, G. trilobus, G. sacculifer	Beta-462597
MOZ4-CSF12	800-801	9,800±30	10,216 - 10,816	10,516	G. ruber, G. trilobus, G. sacculifer	Beta-462598
MOZ4-CSF13	9-11	Modern	Modern	Modern	G. ruber, G. trilobus, G. sacculifer	Beta-462595
MOZ4-CSF13	199-200	1,540±30	667 - 1,104	879	G. ruber, G. trilobus, G. sacculifer	Beta-470561
MOZ4-CSF13	599-601	5,720±30	5,615 - 6,126	5,873	G. ruber, G. trilobus, G. sacculifer	Beta-462596
MOZ4-CSF13	859-860	>43,500	–	–	G. ruber, G. trilobus, G. sacculifer	Beta-470562
MOZ4-CSF13	1200-1201	32,560±200	35,619 - 36,656	36,139	G. ruber, G. trilobus, G. sacculifer	Beta-470563
MOZ4-CSF13	1450-1451	>43,500	–	–	G. ruber, G. trilobus, G. sacculifer	Beta-470564

Table 2: Radiocarbon dates analysed on sediment cores. Calibration with Marine20 curve (Heaton et al., 2020). Reservoir age, ΔR=45, SD=85.

Declaration of interests

The authors declare that they have no known competing financial interests or personal relationships that could have appeared to influence the work reported in this paper.

Highlights

- Early Holocene sliding occurred in contrasting morphological and sedimentary settings

- Two spots of expanded Holocene deposits on the upper slope were emplaced by the interaction between bottom current and the morphology of the margin and of the seabed
- Continuum of sediment undulations ranging from scours to sediment waves from base of slope to upper slope
- On the continental slope the contrast between sedimentation during Bolling-Allerod/Younger Dryas period and the early Holocene is imprinted as a margin wide prominent high amplitude reflector

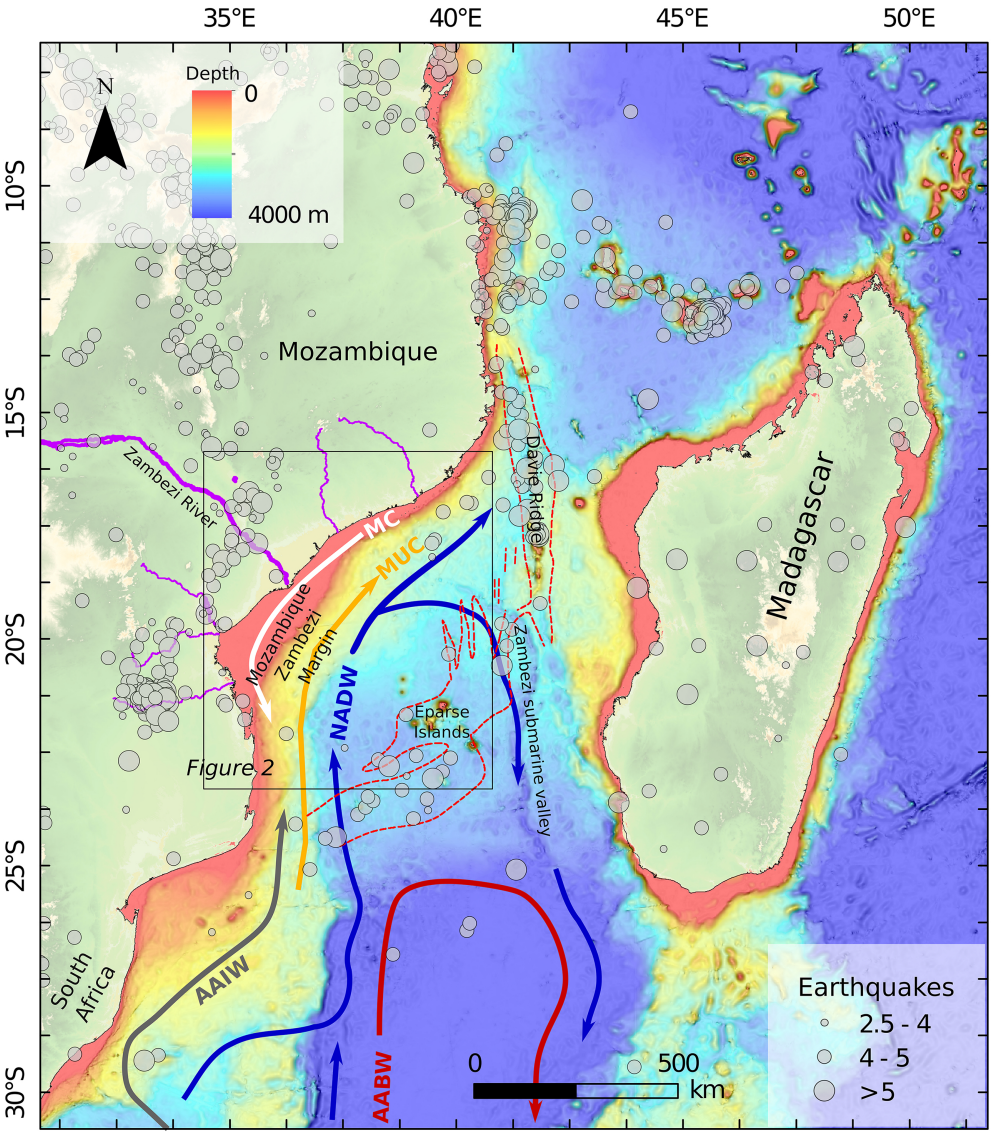
35°E
40°E
45°E
50°E
10°S
15°S
20°S
25°S
30°S
N
Depth
0
4000 m
Mozambique
Madagascar
Zambezi River
Davie Ridge
MC
MUC
Mozambique Zambezi Margin
NADW
Zambezi submarine valley
Eparse Islands
Figure 2
South Africa
AAIW
AABW
0
500
km
Earthquakes
2.5 - 4
4 - 5
>5

Figure 1

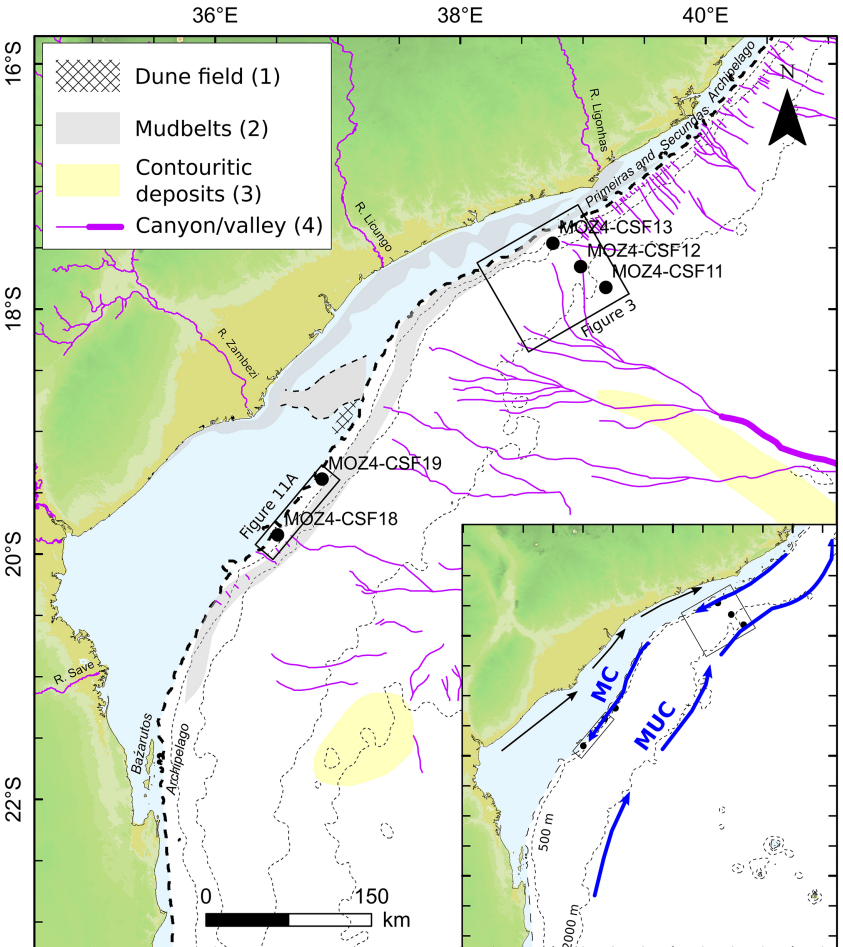
36°E
38°E
40°E
16°S
18°S
20°S
22°S
Dune field (1)
Mudbelts (2)
Contouritic deposits (3)
Canyon/valley (4)
N
R. Ligonhas
Archipelago
Primeiras and Segundas
R. Licungo
MOZ4-CSF13
MOZ4-CSF12
MOZ4-CSF11
Figure 3
R. Zambezi
MOZ4-CSF19
Figure 11A
MOZ4-CSF18
R. Save
Bazaruto Archipelago
0
150
km
MC
MUC
500 m
2000 m

Figure 2

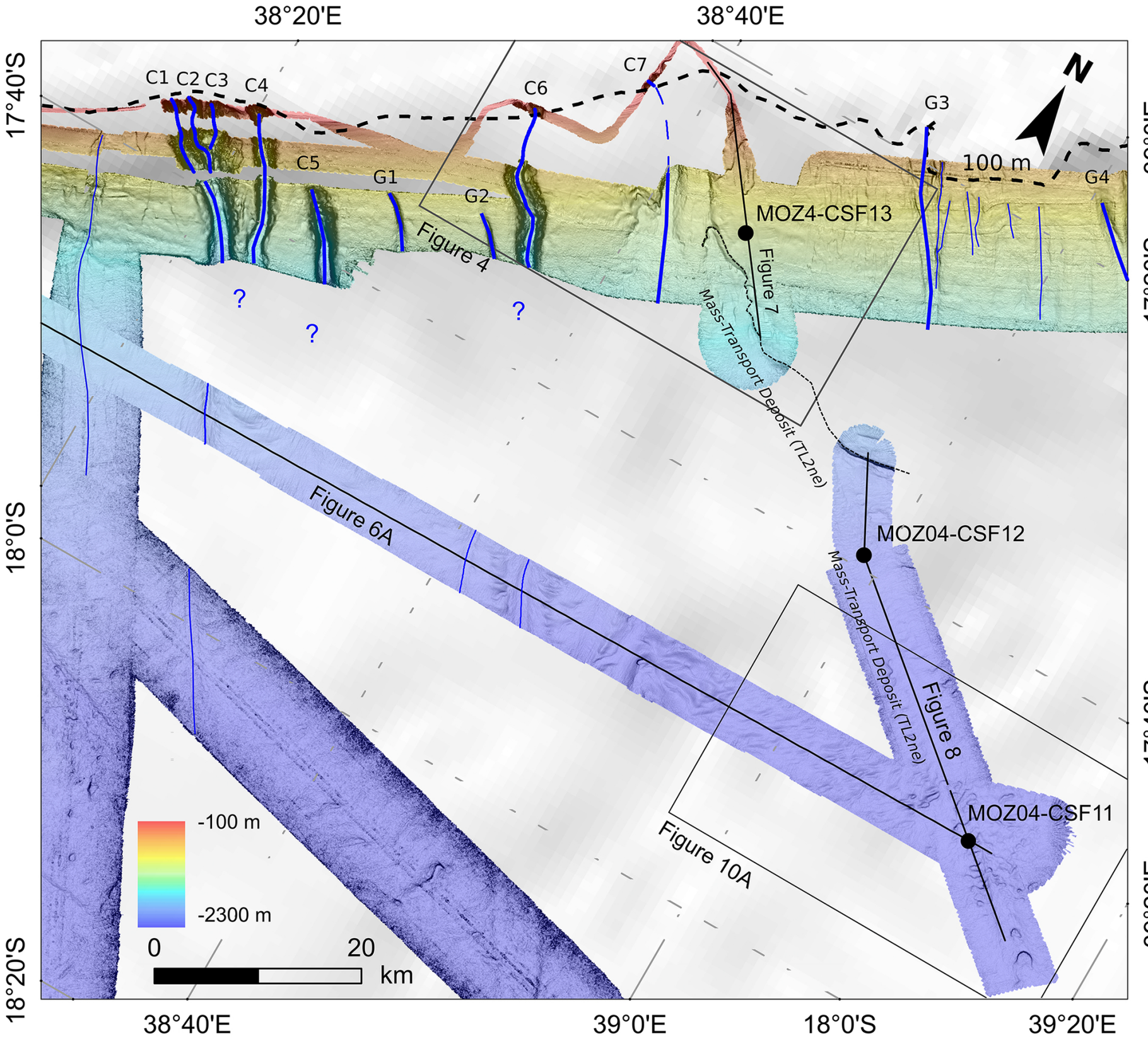
38°20'E
38°40'E
17°40'S
18°0'S
18°20'S
39°0'E
17°20'S
17°40'S
39°20'E
C1
C2
C3
C4
C5
C6
C7
G1
G2
G3
G4
100 m
N
MOZ4-CSF13
MOZ04-CSF12
MOZ04-CSF11
Figure 4
Figure 6A
Figure 7
Figure 8
Figure 10A
Mass-Transport Deposit (TL2ne)
Mass-Transport Deposit (TL2ne)
?
?
?
-100 m
-2300 m
0
20
km

Figure 3

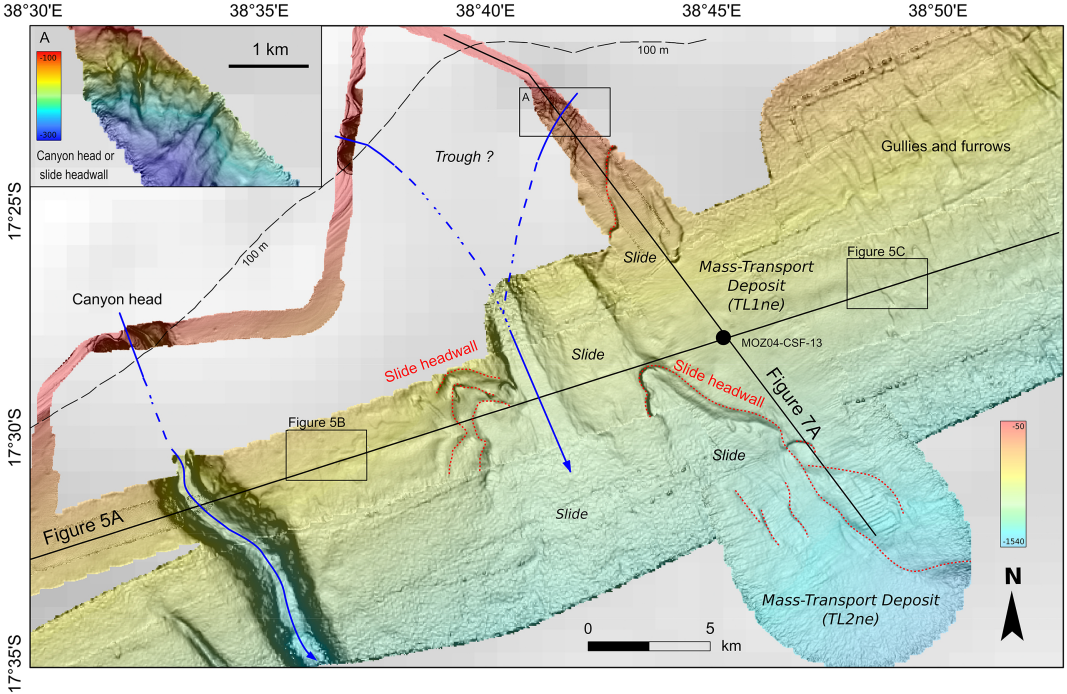
38°30'E
38°35'E
38°40'E
38°45'E
38°50'E
17°25'S
17°30'S
17°35'S
A
-100
-300
1 km
Canyon head or slide headwall
100 m
Trough ?
Gullies and furrows
Slide
Mass-Transport Deposit (TL1ne)
Figure 5C
Canyon head
MOZ04-CSF-13
Slide headwall
Slide
Slide headwall
Figure 7A
Figure 5B
Slide
Figure 5A
Slide
Mass-Transport Deposit (TL2ne)
-50
-1540
N
0
5
km

Figure 4

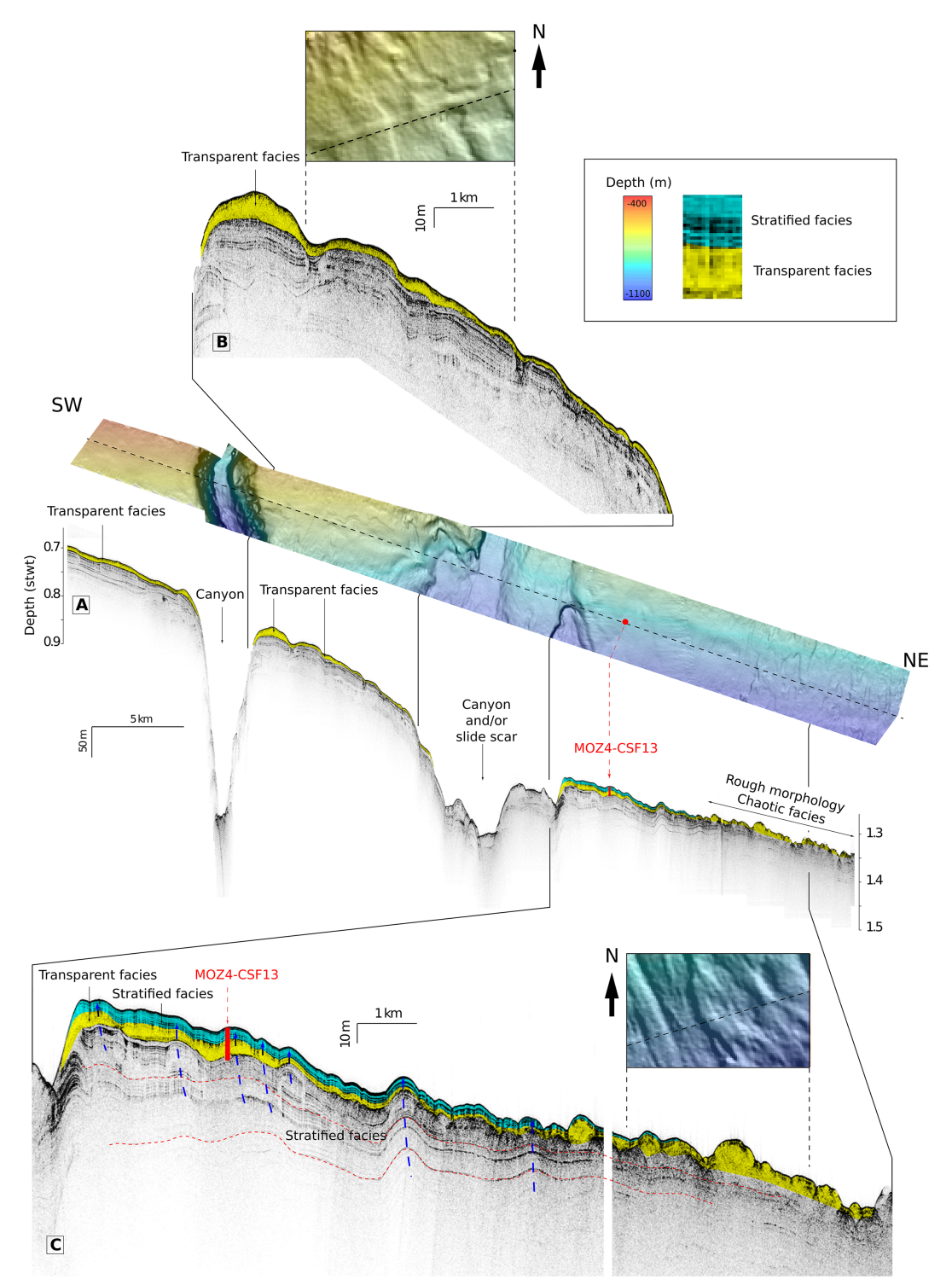
N
Transparent facies
1 km
10 m
Depth (m)
-400
-1100
Stratified facies
Transparent facies
B
SW
NE
Transparent facies
Depth (stwt)
0.7
0.8
0.9
A
Canyon
Transparent facies
5 km
50 m
Canyon
and/or
slide scar
MOZ4-CSF13
Rough morphology
Chaotic facies
1.3
1.4
1.5
Transparent facies
MOZ4-CSF13
Stratified facies
1 km
10 m
N
Stratified facies
C

Figure 5

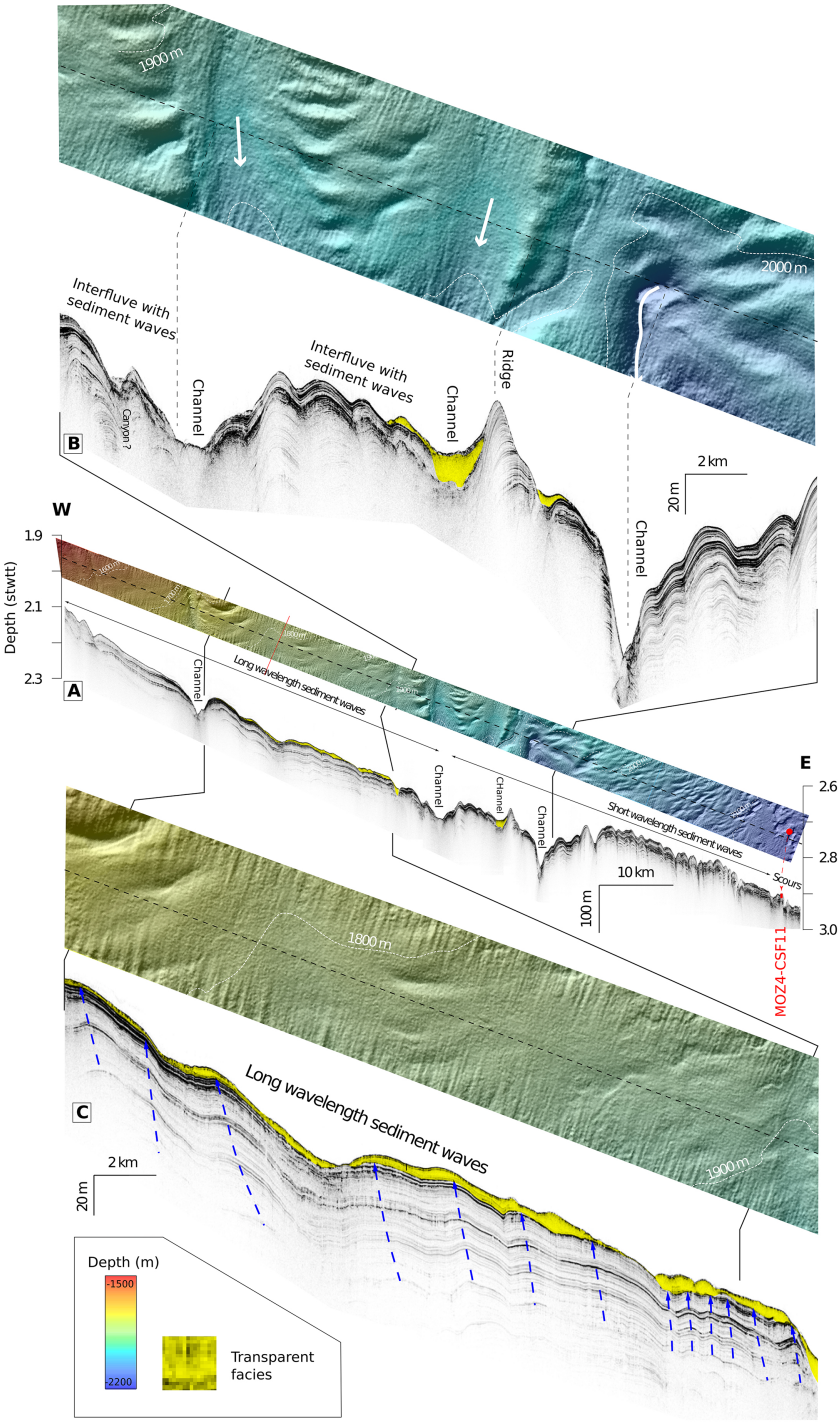
1900 m
2000 m
Interfluve with sediment waves
Channel
Canyon ?
Interfluve with sediment waves
Channel
Ridge
B
2 km
20 m
Channel
W
Depth (stwtt)
1.9
2.1
2.3
A
Channel
Long wavelength sediment waves
Channel
Channel
Channel
Short wavelength sediment waves
E
2.6
2.8
3.0
10 km
100 m
Scours
MOZ4-CSF11
1800 m
Long wavelength sediment waves
C
2 km
20 m
1900 m
Depth (m)
-1500
-2200
Transparent facies

Figure 6

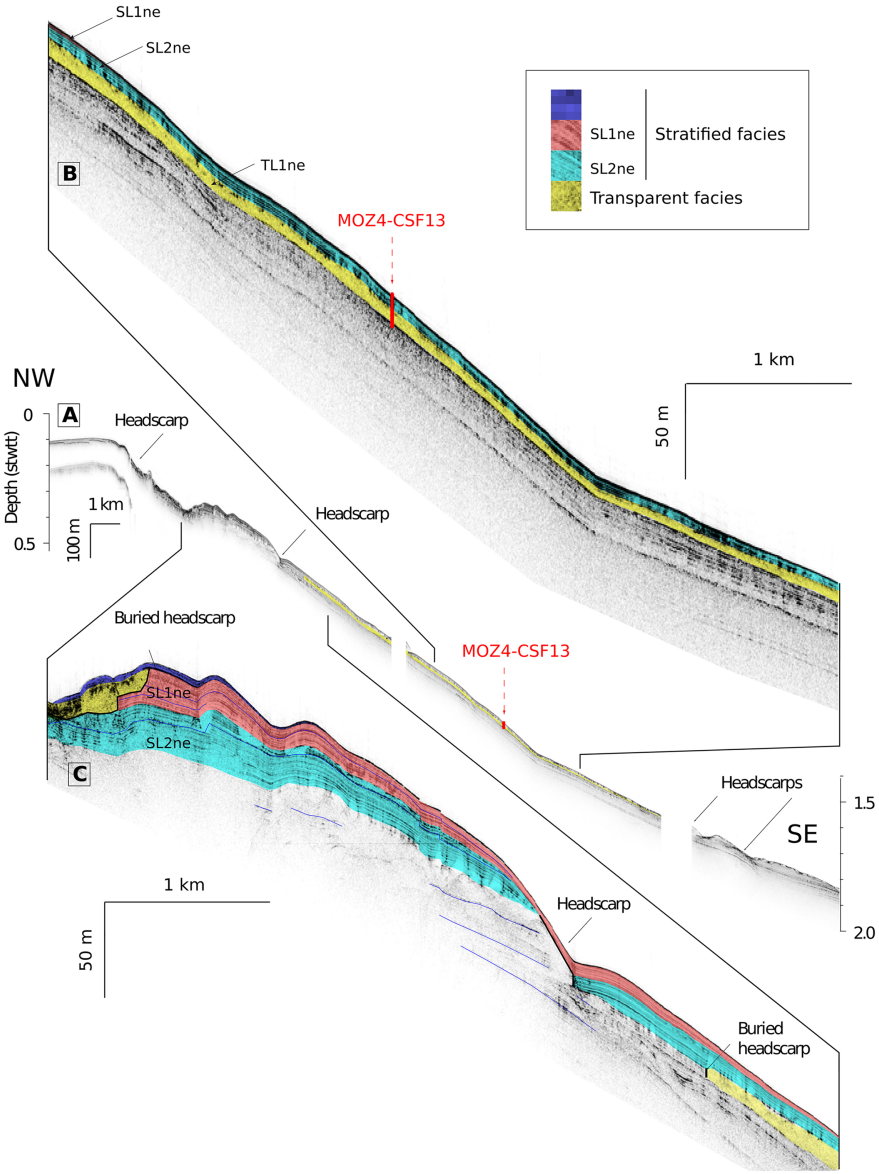
SL1ne
SL2ne
TL1ne
B
MOZ4-CSF13
SL1ne
SL2ne
Stratified facies
Transparent facies
1 km
50 m
NW
A
Depth (stwtt)
0
0.5
Headscarp
1 km
100 m
Headscarp
Buried headscarp
MOZ4-CSF13
SL1ne
SL2ne
C
Headscarps
SE
1.5
2.0
1 km
50 m
Headscarp
Buried
headscarp

Figure 7

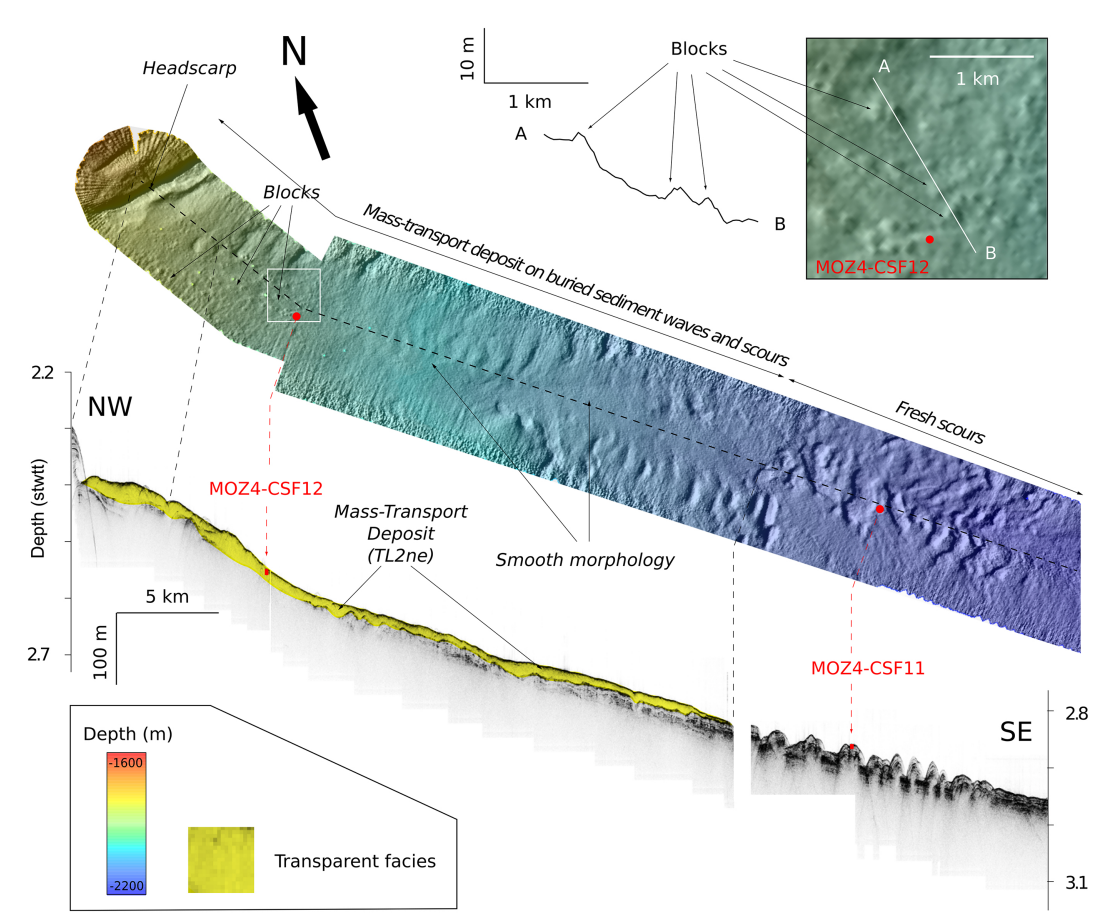
Headscarp
N
Blocks
10 m
1 km
A
B
Blocks
1 km
A
B
MOZ4-CSF12
Mass-transport deposit on buried sediment waves and scours
Fresh scours
2.2
NW
Depth (stwtt)
MOZ4-CSF12
Mass-Transport Deposit (TL2ne)
Smooth morphology
5 km
100 m
2.7
MOZ4-CSF11
SE
2.8
3.1
Depth (m)
-1600
-2200
Transparent facies

Figure 8

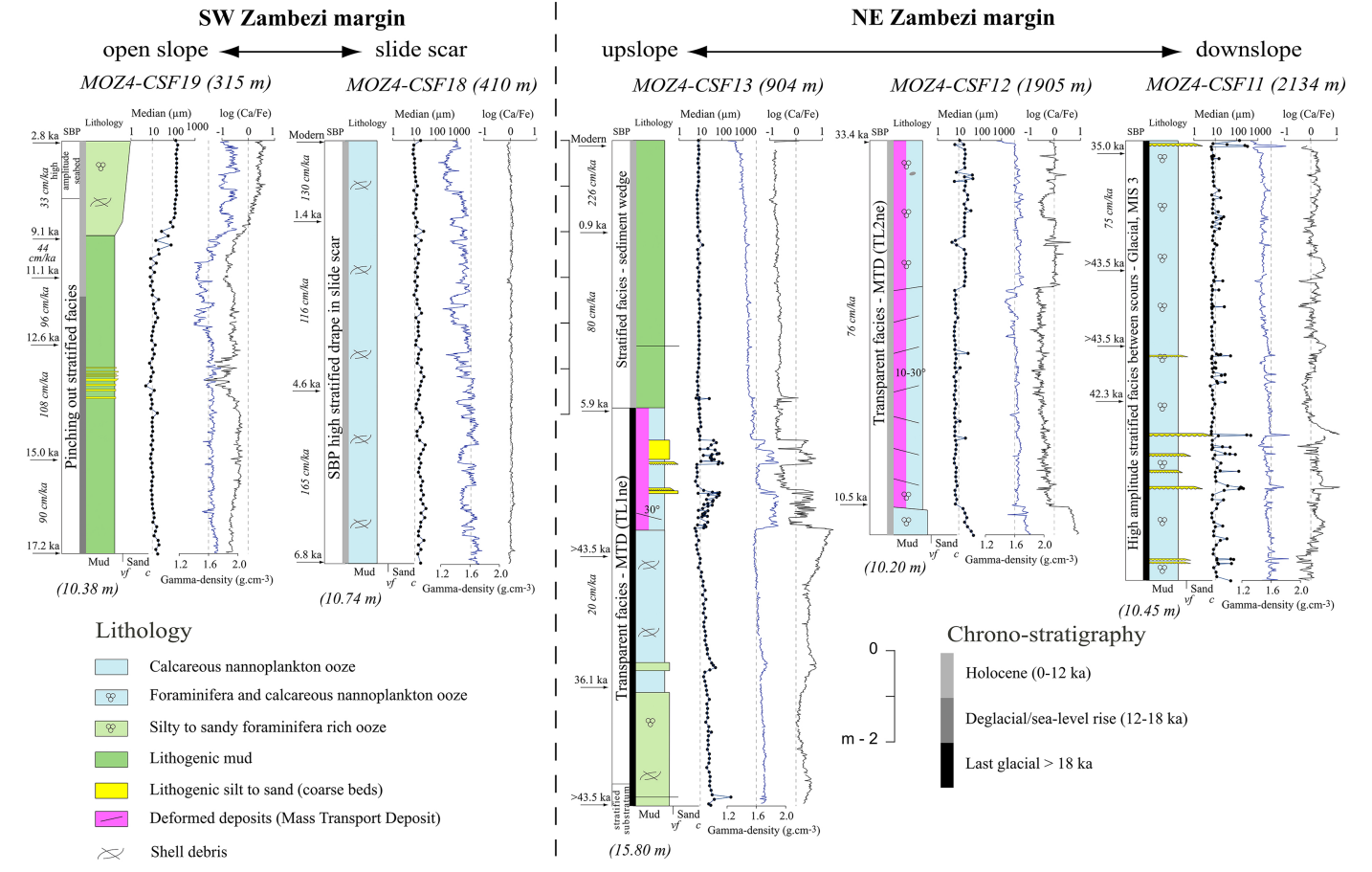
SW Zambezi margin
open slope
slide scar
MOZ4-CSF19 (315 m)
MOZ4-CSF18 (410 m)
NE Zambezi margin
upslope
downslope
MOZ4-CSF13 (904 m)
MOZ4-CSF12 (1905 m)
MOZ4-CSF11 (2134 m)
Lithology
Median (µm)
log (Ca/Fe)
SBP
Gamma-density (g.cm-3)
Pinching out stratified facies
SBP high stratified drape in slide scar
Stratified facies - sediment wedge
Transparent facies - MTD (TL1ne)
Transparent facies - MTD (TL2ne)
High amplitude stratified facies between scours - Glacial, MIS 3
(10.38 m)
(10.74 m)
(15.80 m)
(10.20 m)
(10.45 m)
Lithology
Calcareous nannoplankton ooze
Foraminifera and calcareous nannoplankton ooze
Silty to sandy foraminifera rich ooze
Lithogenic mud
Lithogenic silt to sand (coarse beds)
Deformed deposits (Mass Transport Deposit)
Shell debris
Chrono-stratigraphy
Holocene (0-12 ka)
Deglacial/sea-level rise (12-18 ka)
Last glacial > 18 ka

Figure 9

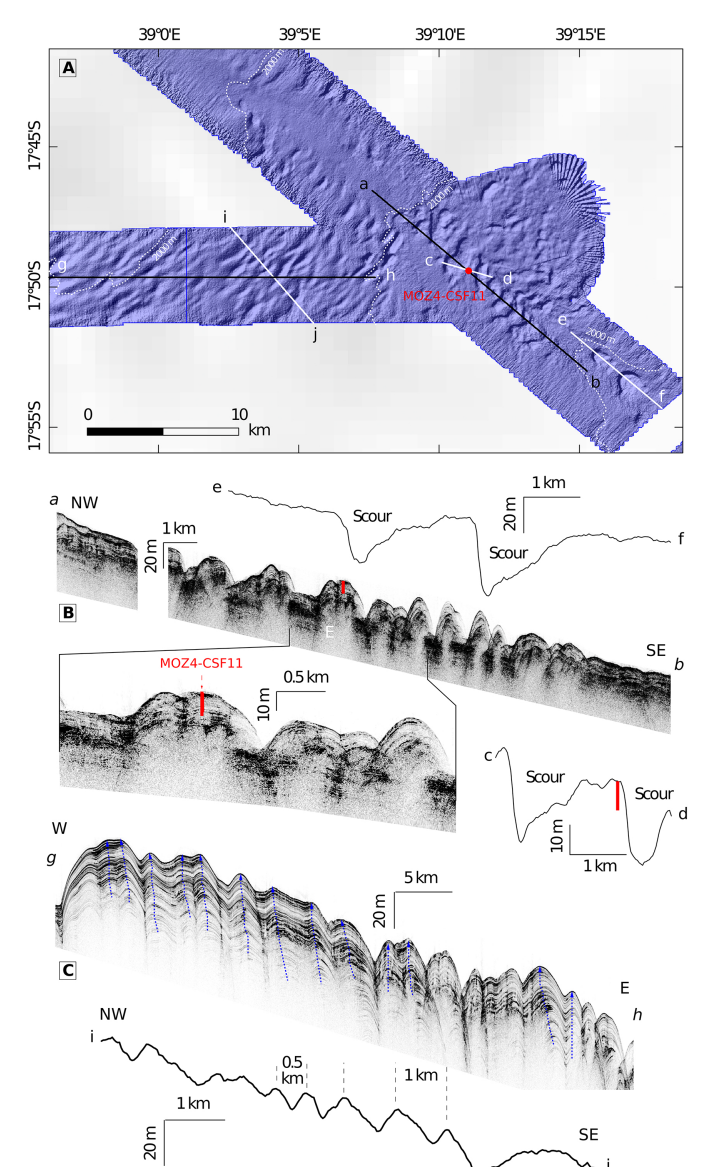
39°0'E
39°5'E
39°10'E
39°15'E
17°45'S
17°50'S
17°55'S
A
a
b
c
d
e
f
g
h
i
j
MOZ4-CSF11
0
10
km
B
NW
SE
Scour
Scour
1 km
20 m
0.5 km
10 m
C
W
E
5 km
20 m
0.5 km
1 km

Figure 10

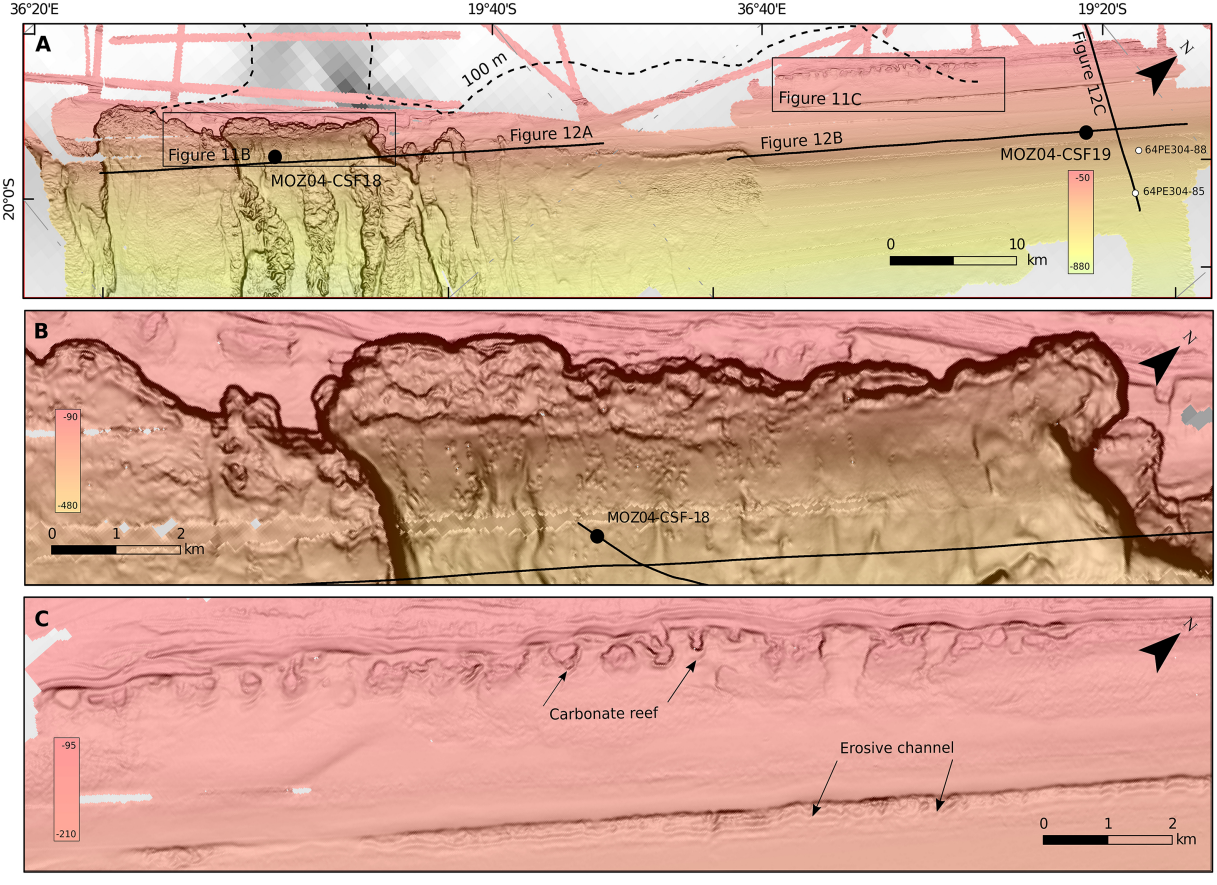
36°20'E
19°40'S
36°40'E
19°20'S
20°0'S
A
100 m
Figure 11B
Figure 11C
Figure 12A
Figure 12B
Figure 12C
MOZ04-CSF18
MOZ04-CSF19
64PE304-88
64PE304-85
-50
-880
0
10
km
B
-90
-480
0
1
2
km
MOZ04-CSF-18
C
Carbonate reef
Erosive channel
-95
-210
0
1
2
km

Figure 11

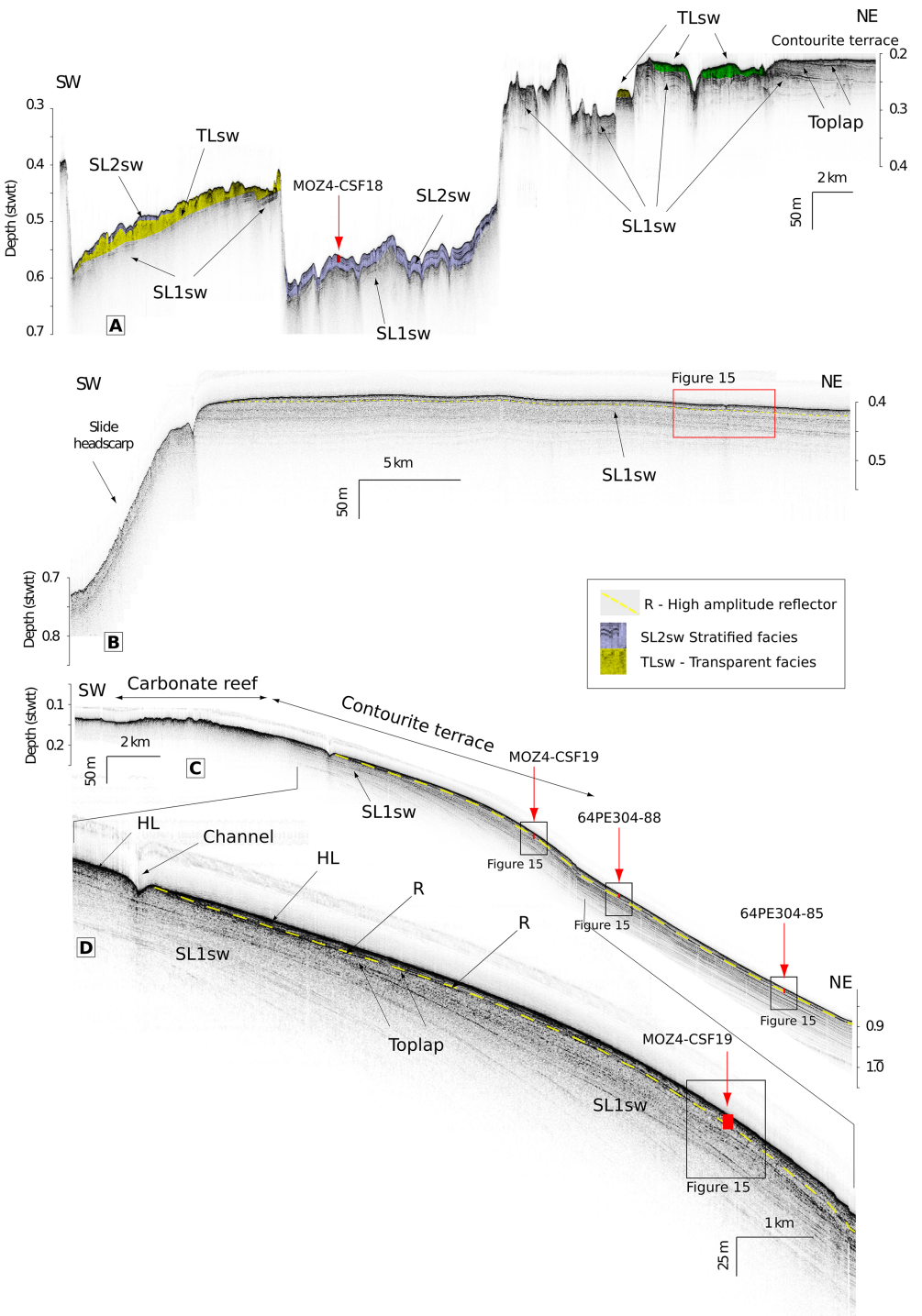
SW
NE
TLsw
Contourite terrace
Toplap
SL2sw
MOZ4-CSF18
SL1sw
2 km
50 m
Depth (stwtt)
A
Slide headscarp
Figure 15
5 km
B
R - High amplitude reflector
SL2sw Stratified facies
TLsw - Transparent facies
Carbonate reef
C
HL
Channel
64PE304-88
64PE304-85
D
1 km
25 m

Figure 12

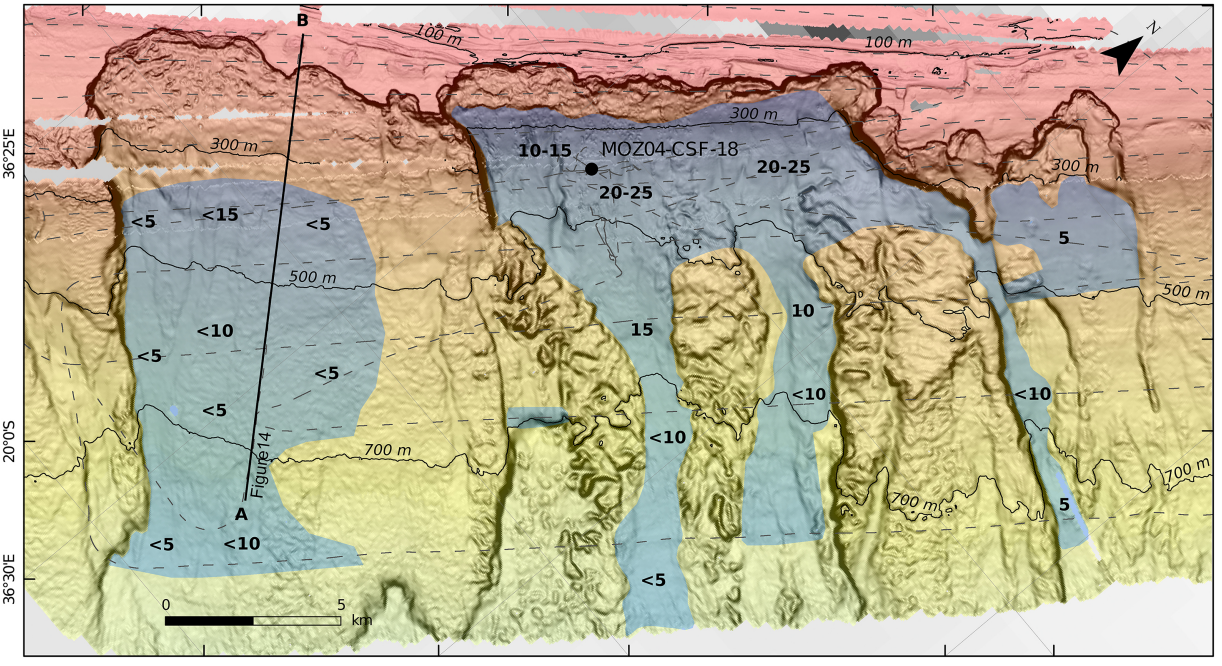
19°55'S
36°25'E
19°50'S
36°30'E
19°45'S
36°25'E
20°0'S
36°30'E
B
A
Figure 14
100 m
300 m
500 m
700 m
MOZ04-CSF-18
10-15
20-25
20-25
<5
<15
<5
<10
<5
<5
<5
<10
15
10
<10
<10
<10
5
5
5
<5
0
5
km

Figure 13

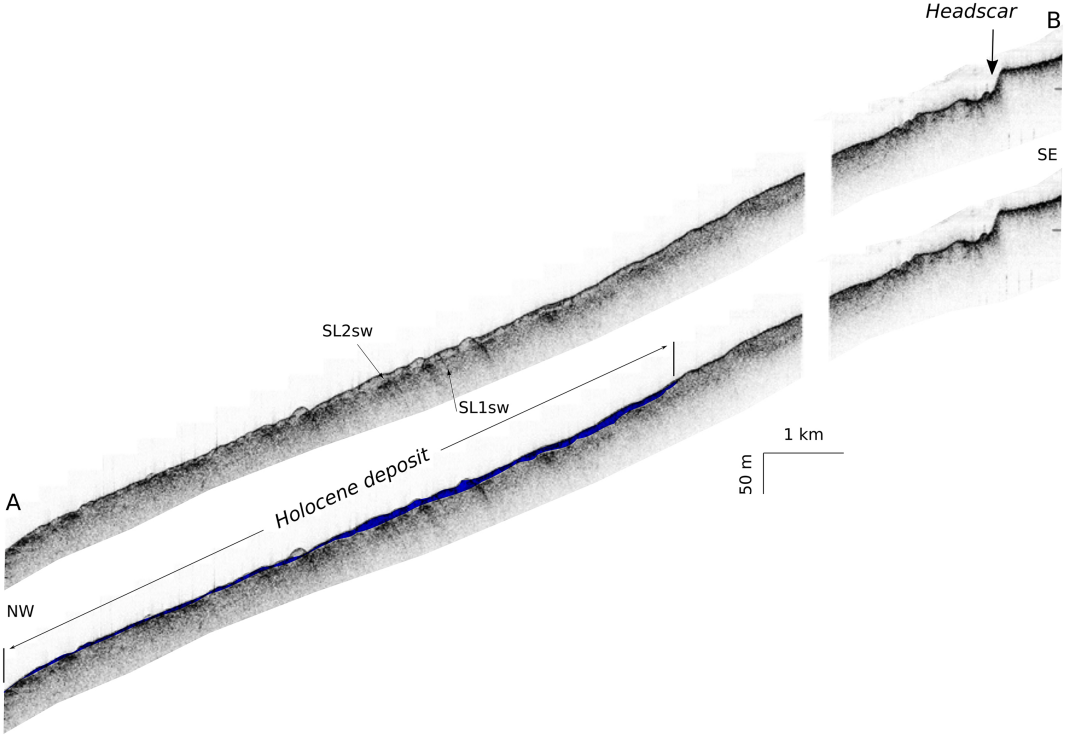

Figure 14

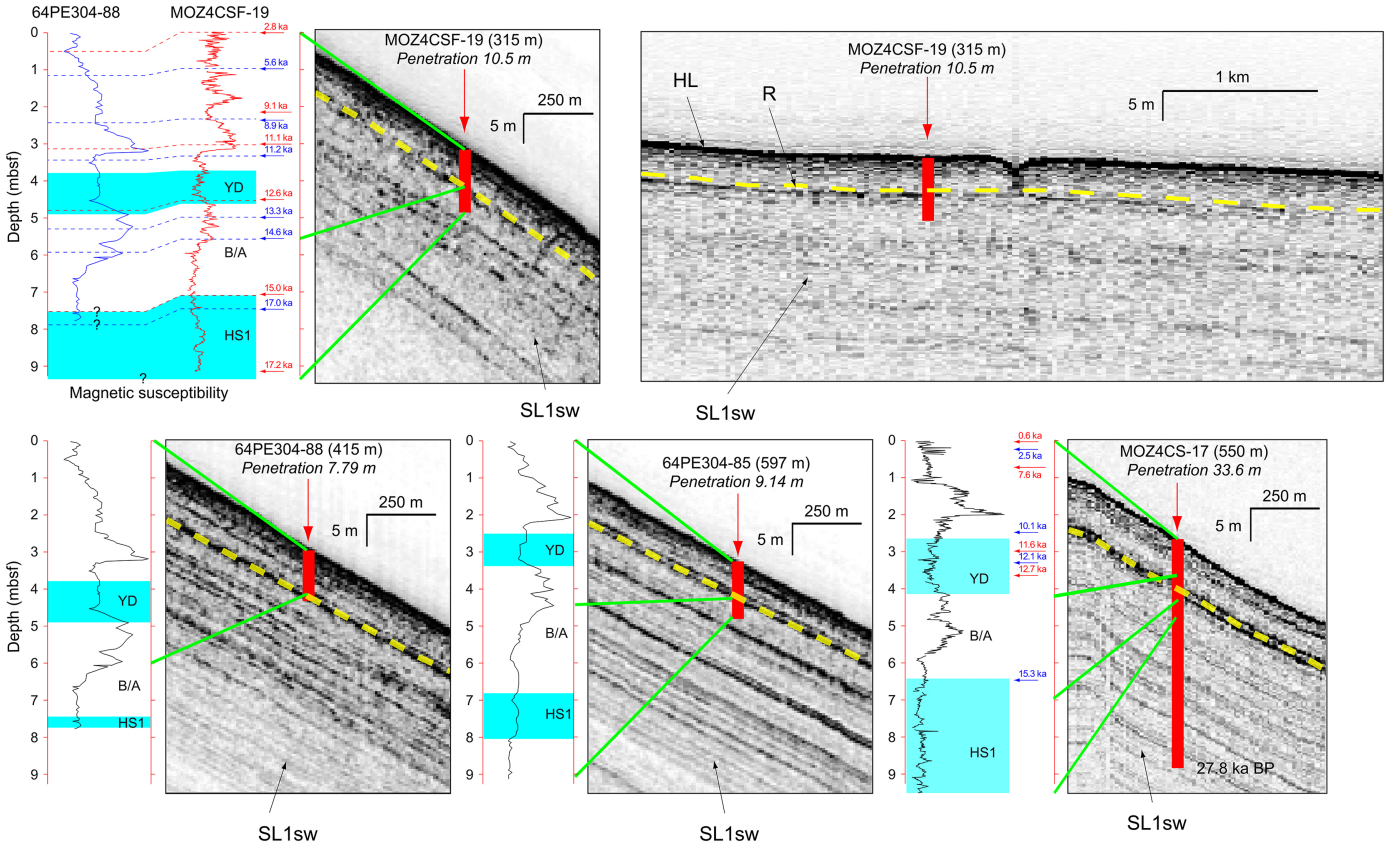
64PE304-88
MOZ4CSF-19
Depth (mbsf)
2.8 ka
5.6 ka
9.1 ka
8.9 ka
11.1 ka
11.2 ka
YD
12.6 ka
13.3 ka
14.6 ka
B/A
15.0 ka
17.0 ka
HS1
17.2 ka
Magnetic susceptibility
MOZ4CSF-19 (315 m)
Penetration 10.5 m
250 m
5 m
SL1sw
HL
R
MOZ4CSF-19 (315 m)
Penetration 10.5 m
1 km
5 m
SL1sw
64PE304-88 (415 m)
Penetration 7.79 m
250 m
5 m
SL1sw
64PE304-85 (597 m)
Penetration 9.14 m
250 m
5 m
SL1sw
0.6 ka
2.5 ka
7.6 ka
10.1 ka
11.6 ka
12.1 ka
12.7 ka
15.3 ka
MOZ4CS-17 (550 m)
Penetration 33.6 m
250 m
5 m
27.8 ka BP
SL1sw

Figure 15

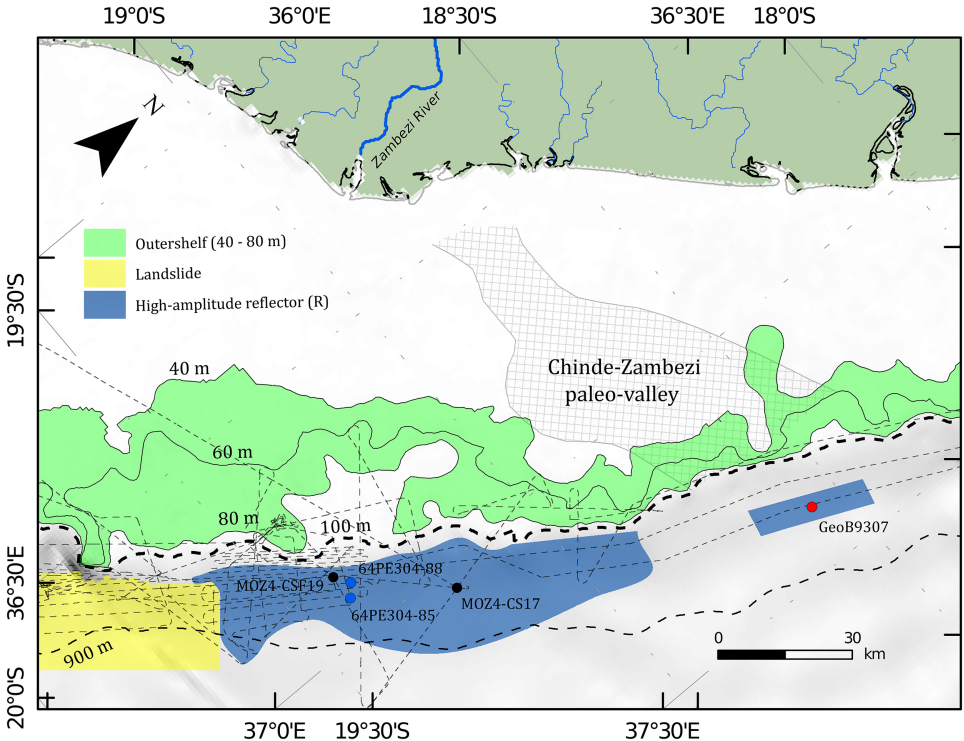
19°0'S
36°0'E
18°30'S
36°30'E
18°0'S
37°0'E
18°0'S
37°30'E
18°30'S
19°30'S
36°30'E
20°0'S
37°0'E
19°30'S
37°30'E
N
Zambezi River
Outershelf (40 - 80 m)
Landslide
High-amplitude reflector (R)
40 m
60 m
80 m
100 m
900 m
Chinde-Zambezi
paleo-valley
GeoB9307
64PE304-88
MOZ4-CSF19
MOZ4-CS17
64PE304-85
0
30
km

Figure 16

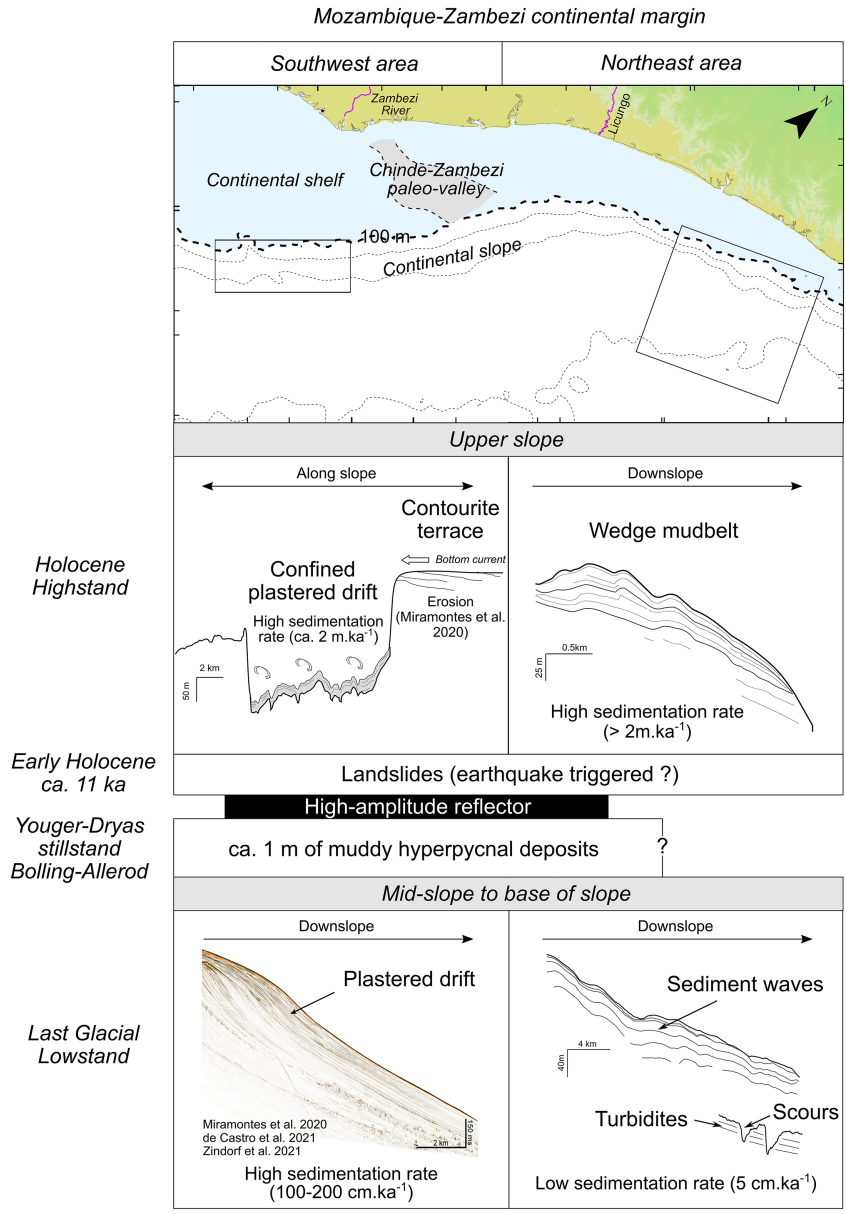
Mozambique-Zambezi continental margin
Southwest area
Northeast area
Zambezi River
Licungo
Continental shelf
Chinde-Zambezi paleo-valley
100 m
Continental slope
Upper slope
Along slope
Contourite terrace
Bottom current
Confined plastered drift
High sedimentation rate (ca. 2 m.ka-1)
Erosion (Miramontes et al. 2020)
2 km
50 m
Downslope
Wedge mudbelt
0.5km
25 m
High sedimentation rate (> 2m.ka-1)
Holocene Highstand
Early Holocene ca. 11 ka
Landslides (earthquake triggered ?)
High-amplitude reflector
Younger-Dryas stillstand Bolling-Allerod
ca. 1 m of muddy hyperpycnal deposits
?
Mid-slope to base of slope
Downslope
Plastered drift
Miramontes et al. 2020
de Castro et al. 2021
Zindorf et al. 2021
2 km
250 ms
High sedimentation rate (100-200 cm.ka-1)
Last Glacial Lowstand
Downslope
Sediment waves
4 km
40m
Turbidites
Scours
Low sedimentation rate (5 cm.ka-1)

Figure 17